RESEARCH ARTICLE

Key Points:
- Secondary eyewall formation in sheared tropical cyclones
- Predictability of SEF and intensity changes of sheared TCs can be very limited
- Coplay of outer rainband, inertial stability, and balanced BL dynamics in SEF

Correspondence to:
F. Zhang,
fzhang@psu.edu

Dynamics and predictability of secondary eyewall formation in sheared tropical cyclones

Fuqing Zhang [iD][1], **Dandan Tao**[1], **Y. Qiang Sun**[1], **and Jeffrey D. Kepert** [iD][2]

[1]Department of Meteorology and Atmospheric Science, Center for Advanced Data Assimilation and Predictability Techniques, Pennsylvania State University, University Park, Pennsylvania, USA, [2]Australia Bureau of Meteorology, Melbourne, Victoria, Australia

Abstract This study examines the predictability and dynamics of tropical cyclone (TC) secondary eyewall formation (SEF), eyewall replacement cycles (ERC), and intensity changes under moderate environmental shear through convection-permitting ensemble simulations. Even with the same environmental shear, the TC intensity changes during formation, rapid intensification, and SEF/ERC can be extremely sensitive to small, unobservable, random initial condition uncertainties, or computer's truncation error due to the chaotic nature of moist convection. Through composite analysis of five ensemble members with similar clear SEF/ERC and diagnostics with a nonlinear boundary layer (BL) model, we identify several key factors in the SEF/ERC process: (1) fast expansion of outer wind fields and changing inertial stability through shear-induced peripheral convection outside of the primary eyewall, (2) downward building and axisymmetrization of the primary (outer) rainband due to enhanced inertial stability and positive feedback between BL and outer convection, (3) establishment of the secondary eyewall along with moat formation that is facilitated by compensating subsidence from the primary eyewall, and (4) weakening and eventual replacement of the original primary eyewall by the strengthening secondary eyewall. It is also seen from the partial ERC cases that the preexisting rainband can be of great importance to the later development of SEF. Diagnosis with the nonlinear BL model shows that the location and relative strengths of the diagnosed frictional updrafts closely match those in the ensemble simulation of the ERC case, suggesting that the boundary layer convergence substantially influences the location of the convection in both eyewalls there.

1. Introduction

Secondary eyewall formation (SEF), during which clouds outside the preexisting eyewall of a tropical cyclone (TC) coalesce to form a new eyewall at a greater radius from the TC center, has long been recognized as a key process for the intensity evolution of a TC [e.g., *Willoughby et al.*, 1982; *Houze et al.*, 2007; *Sitkowski et al.*, 2011]. Typically, as a secondary outer eyewall forms, the intensification of the preexisting inner eyewall slows and usually reverses, causing the storm to weaken. This weakening of the inner eyewall continues as the outer eyewall develops and intensifies. Eventually the inner eyewall dies and is replaced by the outer eyewall, leaving a larger storm, a process that is also termed as the eyewall replacement cycle (ERC)

The motivation to understand and forecast the processes for SEF/ERC is high. SEF can have various consequences arising from dramatic intensity and structure changes mentioned above. At the same time, SEF processes are common in major TCs. Approximately 57% of category 4 and 72% of category 5 TCs in the western North Pacific possess a double eyewall structure [*Kuo et al.*, 2009]. Similarly, *Hawkins et al.* [2006] found 80% of western North Pacific intense typhoons (maximum wind > 120 kt) had concentric eyewalls. Moreover, while the formation of an outer eyewall can cause the storm to weaken temporarily, the larger hurricane after the eyewall replacement process typically has broadened wind fields with enhanced integrated kinetic energy [*Maclay et al.*, 2008] that may induce larger damage.

Many hypotheses on SEF have been proposed, including, but not limited to, (a) two-dimensional vortex interactions [*Kuo et al.*, 2008], (b) radiation of vortex Rossby waves (VRWs) and the associated wave-mean flow interaction near the critical radius [*Montgomery and Kallenbach*, 1997; *Abarca and Corbosiero*, 2011; *Menelaou et al.*, 2012], (c) dynamic adjustment, mostly balanced, to latent heating outside the primary

eyewall [*Rozoff et al.*, 2012; *Fang and Zhang*, 2012; *Sun et al.*, 2013], (d) unbalanced dynamics associated with boundary layer processes [*Huang et al.*, 2012; *Abarca and Montgomery*, 2013; *Wang et al.*, 2013], and (e) a feedback between boundary layer convergence and convective vorticity tendency [*Kepert*, 2013; *Kepert and Nolan*, 2014]. However, the two-dimensional vortex interaction hypothesis was questioned in *Moon et al.* [2010]; the role of unbalanced boundary layer dynamics in SEF was challenged by balanced boundary layer dynamics [*Sun et al.*, 2013]. So far there is still no clear consensus on the fundamental physics behind the SEF process [*Wu et al.*, 2016].

Recently the role of outer rainbands on SEF has gained more and more attention through successful modeling experiments and/or simulations. *Judt and Chen* [2010] first noticed that the potential vorticity generation and accumulation at the rainband region could lead to the SEF. *Qiu and Tan* [2013] pointed out that the outer rainbands could induce asymmetric boundary layer inflow that penetrates into the inner-core region, reinforces convergence at the leading edge of the strong inflow, and lifts up the moist air there. More recently, *Zhu and Zhu* [2014] argued that for SEF to occur, the diabatic heating generated by the outer rainband convection must reach a critical strength relative to that of the eyewall convection. The importance of latent heating from the outer rainbands is also discussed in *Moon and Nolan* [2010], *Fang and Zhang* [2012], and *Sun et al.* [2013].

Another key factor gaining a lot of attention to understand SEF/ERC process is the dynamics of the hurricane boundary layer. *Zhang et al.* [2011] found that the secondary wind maximum associated with the SEF generally shows up in the boundary layer where the moist air is lifted out of the layer. Despite widely acknowledged importance of the boundary layer, different views on its dynamic roles exist. *Huang et al.* [2012] proposed that the unbalanced supergradient flow is critical for initiating and sustaining the deep convection outside the primary eyewall (also referred by *Abarca and Montgomery* [2013]). *Kepert* [2013] argued that the supergradient flow is not essential to SEF through exploring an Ekman-like boundary layer model, but instead he proposed that the boundary layer convergence was the result from a region of locally stronger radial gradient of the gradient wind vorticity. Different from all these theories, *William et al.* [2013] hypothesized that the secondary eyewall might be interpreted as a "shock-like" structure similar to that of the solution of Burgers' equation in the boundary layer, although *Williams* [2015] subsequently showed that these shocks were an artifact of the slab model [see also *Kepert*, 2010a, 2010b].

Along with the lack of a consensus physical understanding of the SEF, accurate forecasting of the SEF is challenging. Current forecast attempts are based more on empirical equations and statistical tools [*Kossin and Sitkowski*, 2009]. *Zhang and Tao* [2013] showed that the intensity and rapid intensification process of a TC can be extremely sensitive to small-scale, small-amplitude initial-condition uncertainties under vertical shear. It is of interest to know whether the SEF share similar uncertainties. *Judt et al.* [2016] indicates that the predictability of the TC vortex is dependent on its scale. As SEF reflects on the mean vortex scale, it might have a longer prediction time than the smaller convective-scale processes.

This study aims to examine the predictability and dynamics of tropical cyclone SEF/ERC and its intensity changes through a series of convection-permitting ensemble simulations. An ensemble study with multiple simulations of the SEF/ERC also helps to reduce the case dependency in the statistics. We will also explore the dynamic role of the boundary layer using the nonlinear boundary layer model developed in *Kepert and Wang* [2001]. Section 2 introduces the experimental design and the tools used in the study. Section 3 explores the predictability behavior of the SEF/ERC in all the members. An in-depth analysis of five selected members that undergo similar clear SEF/ERC is presented in section 4. Analysis of another five selected members that have partial ERC is shown in section 5. Section 6 shows the diagnostic results using the boundary layer model. Summary is given in section 7.

2. Experimental Design

2.1. Model Setup for the WRF Idealized Simulation

The Advanced Version of the Weather Research and Forecast (WRF) model version 3.1.1 with a 2 km grid spacing for the innermost nest is used whose configuration is exactly the same as the "SH6" ensemble simulation in *Tao and Zhang* [2015] following *Zhang and Tao* [2013]. The ensemble is initialized with the same idealized modified Rankine vortex that has a maximum surface wind speed of 15 m s^{-1} at 135 km radius. The "point-downscaling" method developed in *Nolan* [2011] is used to add a westerly vertical shear of 6 m s^{-1} (but with
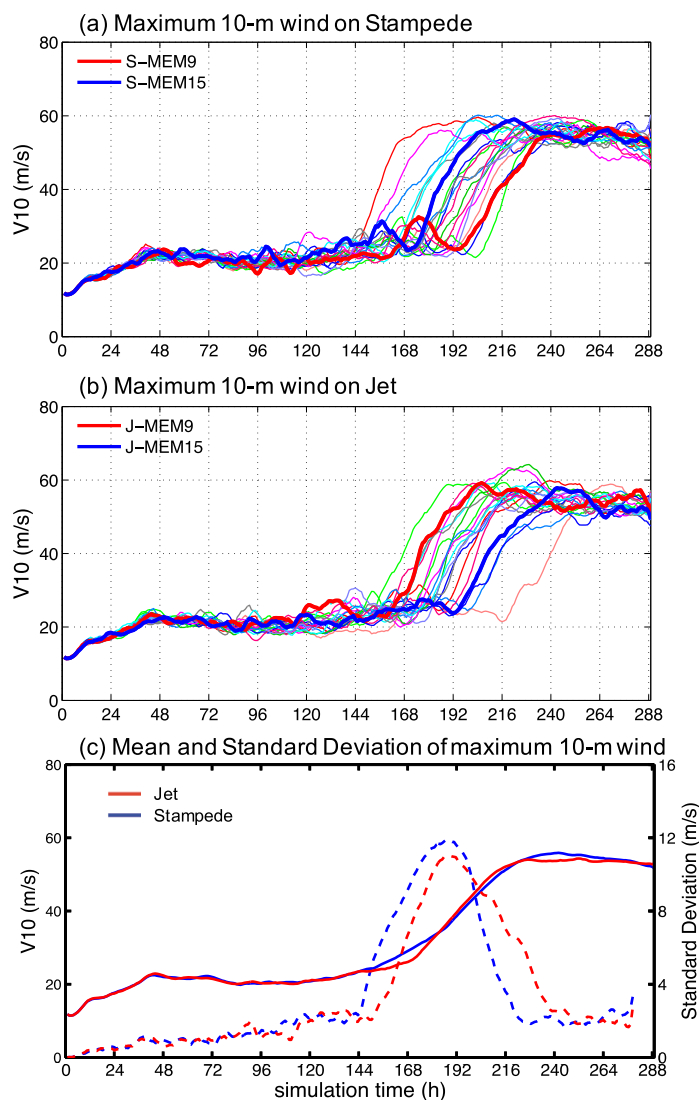
Figure 1. Evolution of maximum 10 m wind (running smoothed) of (a) SH6 on Stampede and (b) SH6 on Jet. Lines with same color are the simulations with same initial condition; (c) mean (solid line) and standard deviation (dash line) of 10 m wind for two sets.

no temperature gradient); the vertical shear profile is shown in *Tao and Zhang* [2015, Figure 1]. The *Dunion* [2011] mean hurricane season sounding is used for the environmental moisture and temperature profile while a constant sea surface temperature (27°C) and a constant Coriolis parameter equivalent to 20°N are used. The ensemble with this setup was denoted as SH6 in *Tao and Zhang* [2015]. As in *Zhang and Tao* [2013], within each ensemble, exactly the same environment conditions but different realizations of moisture perturbations with magnitude randomly selected from a uniform distribution of (−0.5, 0.5) g kg^{-1} are applied to all the model grid points below 950 hPa within the innermost domain. To examine the sensitivity of hurricane prediction to computer compiler and/or architecture, this same set of 20 ensemble perturbations is used for initializing the WRF simulations with the model configurations at both the "Stampede" computer cluster at the Texas Advanced Computer Center (TACC) and the "Jet" computer cluster at the Earth System Research Laboratory (ESRL) of NOAA.

For further understanding the SEF/ERC dynamics, we select five members with clear SEF and perform an in-depth composite analysis (denoted as "FullERC"). In comparison, we also perform the composite analysis of another five selected members that only have partial secondary eyewall formation and eyewall replacement cycle (hereafter denoted as "PartERC").

2.2. Boundary Layer Diagnostic Calculations

To diagnose the contribution of frictional convergence to the near-surface vertical motion, we use the diagnostic boundary layer model of *Kepert and Wang* [2001]. This model diagnoses the steady state boundary layer flow in response to an applied pressure field by integrating the momentum and thermodynamic equations forward in time until a nearly steady state is attained, while holding the imposed pressure field at the top of the model fixed. The free atmosphere forces the boundary layer only through the applied pressure field, with other influences such as convective downdrafts being neglected. Any feedback from the boundary layer to the imposed pressure field is likewise neglected. The model budget equations include the effects of surface friction and vertical turbulent diffusion, with a variety of parameterizations available to represent these processes, as well as horizontal and vertical advection and the pressure gradient force. Similar models have been recently developed by *Gao and Ginis* [2014] and *Williams* [2015].

The ensemble-mean gradient wind data at hourly intervals at 2.25 km height were extracted from the five-member composite for the FullERC and PartERC members, respectively, and provided to the KW01 model. This is the only data passed between the two models. This 2.25 km height was chosen because it is representative of the pressure gradient in the boundary layer and is close to the top boundary of the KW01 model. The KW01 model is integrated for 24 h to a quasi-steady state, and the data azimuthally averaged, for each hour of each ensemble composite. There are 20 vertical levels, with the lowest few at 10, 22.8, and 39 m and the highest at 2.25 km. The maximum vertical spacing is 200 m and the horizontal grid spacing is 3 km. We use the same surface roughness parameterization as used in the WRF ensemble (isftcflx =1 in WRFV3.1.1). The YSU-like turbulence parameterization from *Kepert* [2012] was used, with a fixed depth of 750 m, as in *Kepert and Nolan* [2014]. This parameterization was modified to increase the diffusivity above that depth in a similar way to that in *Kepert and Nolan* [2014] and for similar reasons, except that the diffusivity aloft was given about half the value used by *Kepert and Nolan* [2014]. This change increases the vertical wind shear above the inflow layer and improves the agreement with the WRF simulation. However, it has only a minor effect on the distribution or strength of the frictional updraft, since most of the horizontal convergence occurs near the surface.

3. Intrinsic Predictability and the "Butterfly Effect": Sensitivity to Different Computers

This is a follow-up of our recent studies of *Zhang and Tao* [2013] and *Tao and Zhang* [2015] which examine the formation and predictability of sheared tropical cyclones (TCs) and found their intensity can be extremely sensitive to small-scale, small-amplitude initial-condition uncertainties. Among the set of ensembles examined with sea surface temperature of 27°C in *Tao and Zhang* [2015], the forecast uncertainty is the largest for the ensemble SH6 with the shear value of 6 m s^{-1} for which the rapid intensification (RI) time between members can differ as much as 3 days (Figure 1a). Moreover, the limited predictability of the sheared tropical cyclones can be exemplified not only by the extreme sensitivity to small-amplitude initial-condition perturbations [*Zhang and Tao*, 2013; *Tao and Zhang*, 2015], but can also be seen through equally strong divergence between pairs of simulations that have exactly the same initial perturbations but performed on two different computer clusters. For example, the simulations shown in Figure 1a were performed on the Stampede cluster at the Texas Advanced Computer Center while the simulations in Figure 1b were performed on the Jet cluster at the Earth System Research Laboratory of NOAA. As a highlight, despite using exactly the same initial perturbation, model configuration and number of computer cores, ensemble member #9 on Stampede (S-MEM9) is one of the slowest developing members (with RI starting around 204 h, thick red line, Figure 1a) but the same member (J-MEM9) is one of the earliest developers among the ensemble simulated on Jet (with RI starting around 168 h, Figure 1b). Similar divergence can be seen between two simulations of member 15 (thick blue curves) and to a lesser degree for other members (Figure 1a versus Figure 1b). This is consistent with the simulations under 5 m s^{-1} vertical wind shear (SH5) on Stampede and Ranger clusters at the Texas Advanced Computer Center [*Tao and Zhang*, 2015] indicating that this phenomenon is not accidental.

The divergence between simulations with the same initial perturbation using the same forecast model is reminiscent of the well-known serendipity encountered by Professor Edward Lorenz in 1963 which led to the discovery of "deterministic chaos" [*Lorenz*, 1963], arguably the most important contribution in atmospheric predictability. Nevertheless, the ensemble mean and standard deviation of the 10 m maximum wind speed for each of the two 20-member ensembles on different computers are strikingly similar (Figure 1c), which indicates ensemble and probabilistic forecasting is an effective approach dealing with (deterministic) limit of predictability.

Figures 2 and 3 show pairwise comparisons of the azimuthally averaged vertical motion and tangential wind at 1 km for each member with the same initial conditions but performed on the two different computers, which further demonstrate the divergence of TC intensity and structure through running the same model on different computers beyond differences in small initial perturbations. Moreover, besides the difference in formation and RI, the spread among simulations (and thus the limit of TC predictability) can in some instances also be seen in the timing and strength of the eyewall replacement cycles (ERC): some members exhibit the clear signature of secondary eyewall formation (SEF), some have partial ERC (or even
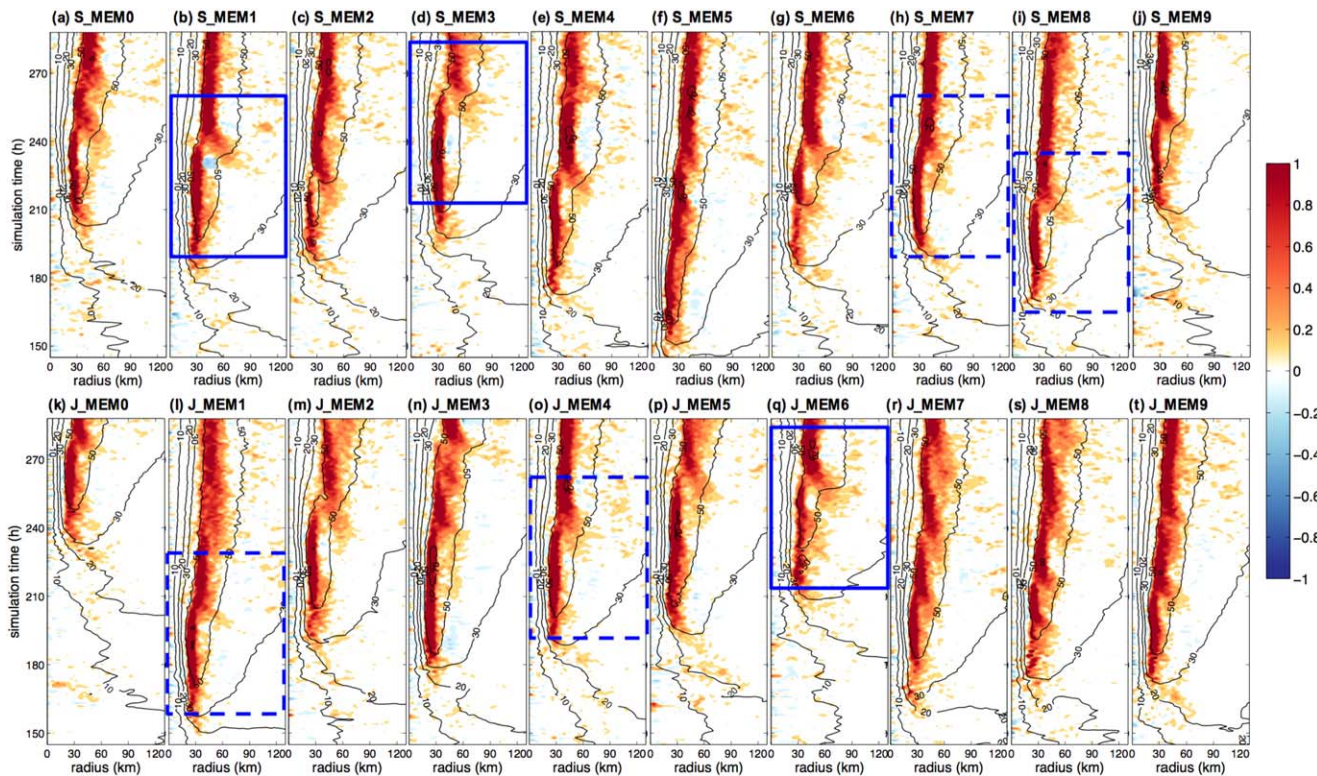
Figure 2. Vertical (shading, m s^{-1}) and tangential (contour, m s^{-1}) wind at 1 km for (a–j) member 0–9 on Stampede and (k–t) member 0–9 on Jet. Blue solid box for members with full eyewall replacement cycle, blue dash box for members with partial eyewall replacement cycle.
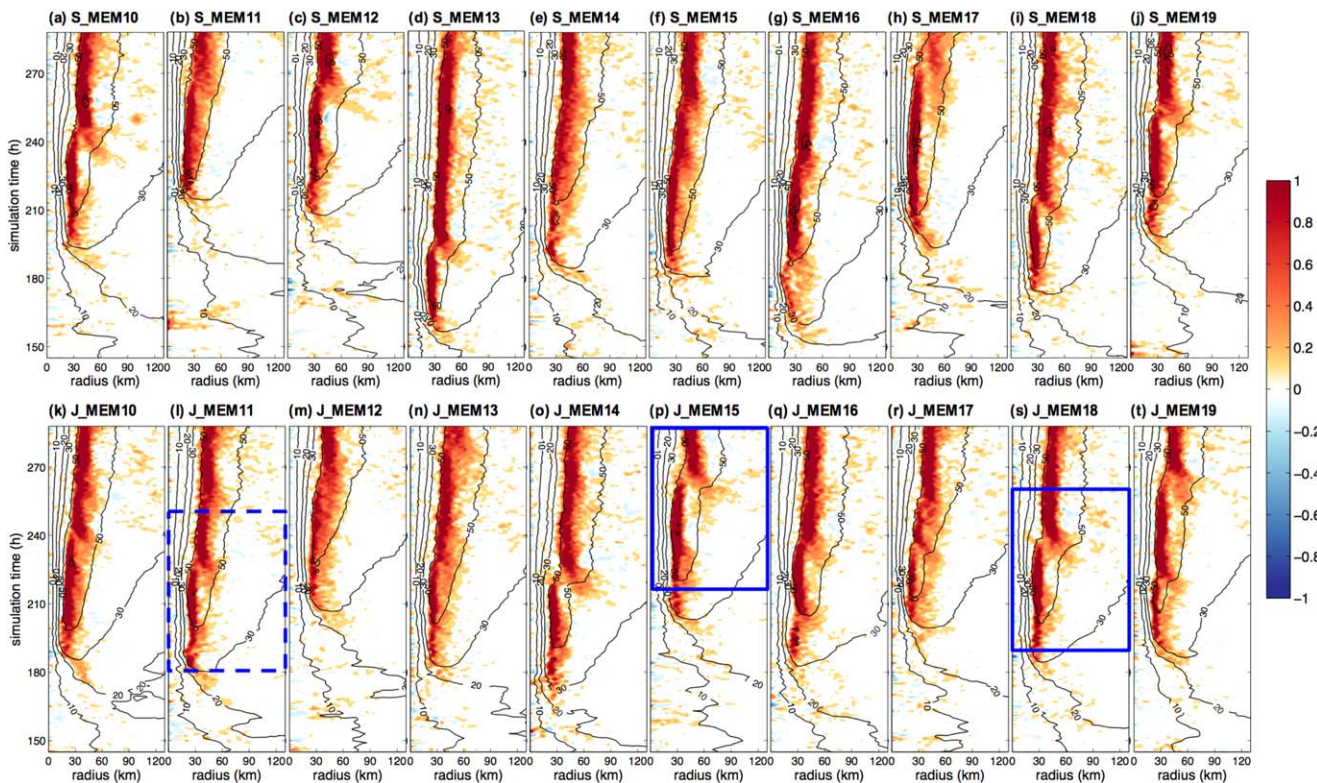
Figure 3. Vertical (shading, m s^{-1}) and tangential (contour, m s^{-1}) wind at 1 km for (a–j) member 10–19 on Stampede and (k–t) member 10–19 on Jet. Blue solid box for members with full eyewall replacement cycle, blue dash box for members with partial eyewall replacement cycle.
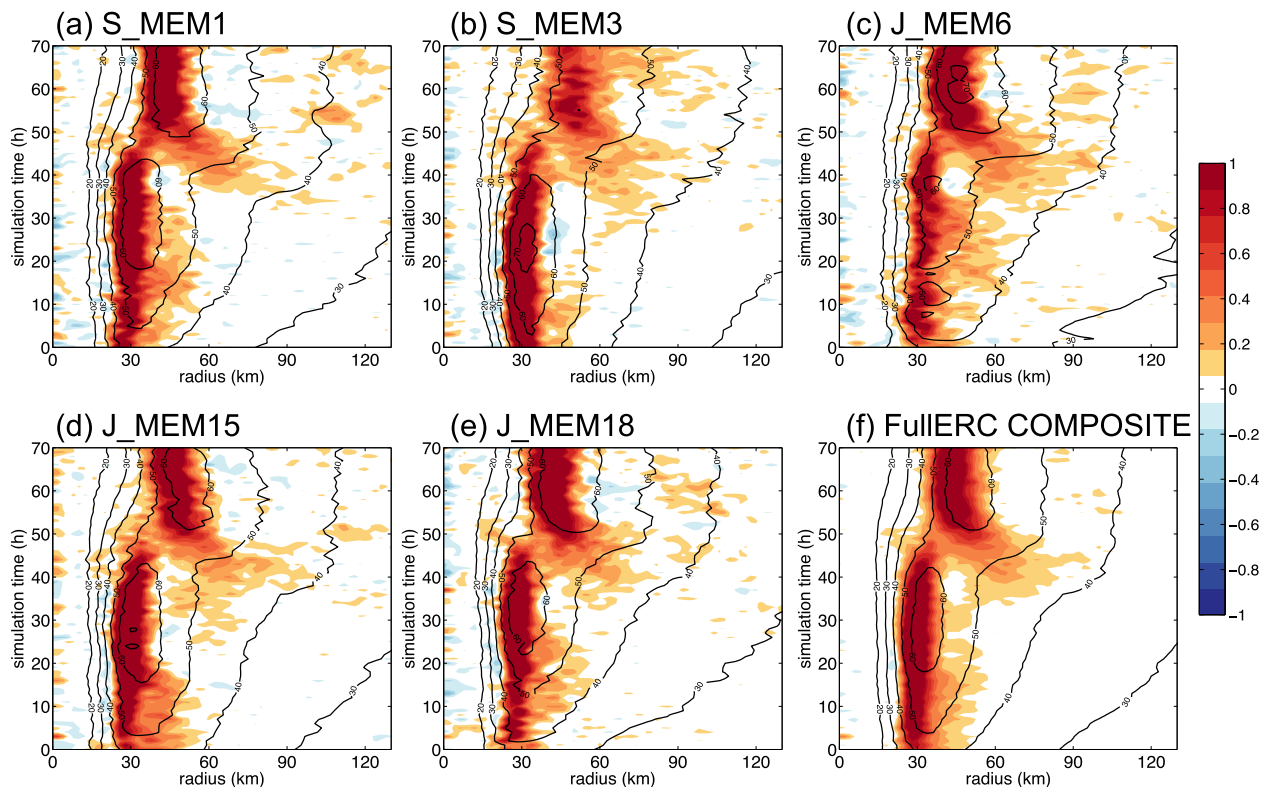
Figure 4. Vertical (shading, m s^{-1}) and tangential (contour, m s^{-1}) wind at 1 km for (a) member 1 on Stampede (S_MEM1); (b) member 3 on Stampede (S_MEM3); (c) member 6 on Jet (J_MEM6); (d) member 15 on Jet (J_MEM15); and (e) member 18 on Jet (J_MEM18). (f) Vertical and tangential wind composite of five ensembles (hereafter FullERC) at 1 km. The time is rescaled to match the SEF process between 40 and 50 h.

multiple episodes) while others may have no ERC at all (S_MEM14 and J_MEM12), despite the same environmental conditions being used for all these simulations. Under exactly the same environment, the variability in SEF/ERC among ensemble members are primarily due to processes internal to the TC itself, as also noted by *Kossin and DeMaria* [2016]. Nevertheless, since nearly all members (38 out of 40) undergo ERC or partial ERC, the moderately sheared environmental conditions for this ensemble are apparently favorable for SEF/ERC. In most of the members, the first episode of either full ERC or partial ERC is observed to begin right after the completion of RI which usually lasts about 1–2 days.

4. Composite Analysis of Five Selected Members With Clear SEF/ERC

To further examine the dynamics and predictability of the SEF and ERC, Figure 4 presents a zoomed-in view of the five members that have the clearest indicators of SEF (clear secondary updraft maximum outside primary updraft, clear moat, clear extension of outer tangential wind field), along with their composite, from around 40 h before the start of the SEF until around 20 h after the ERC completes for a total timespan of 70 h (as denoted by the blue box on these members in Figures 2 and 3). For convenience of presentation, hereafter we denote the five-member composite as "FullERC" and the start of this timespan as the new "0" hour for each of these five members and their composite shown in Figure 4, and the subsequent hour of simulation is after this start time. As will become clear later, the SEF begins around 20–30 h while the ERC completes between 40 and 50 h in the new composite time coordinate.

Figure 5 shows the horizontal map view of the simulated radar reflectivity and vertical velocity fields at 3 km height at selected times for the FullERC composite. At 35 h, despite an abundance of peripheral convection and a loosely defined spiral rainband, the strongest updraft is located at the primary eyewall between 30 and 40 km radius from the composite TC center (Figure 5d); there is only one local maximum of azimuthally averaged reflectivity near the strongest updraft in the composite (Figures 4f and 5a) and each member (Figures 4a–4e). By 40 h, significant strengthening and axisymmetrization of the outer
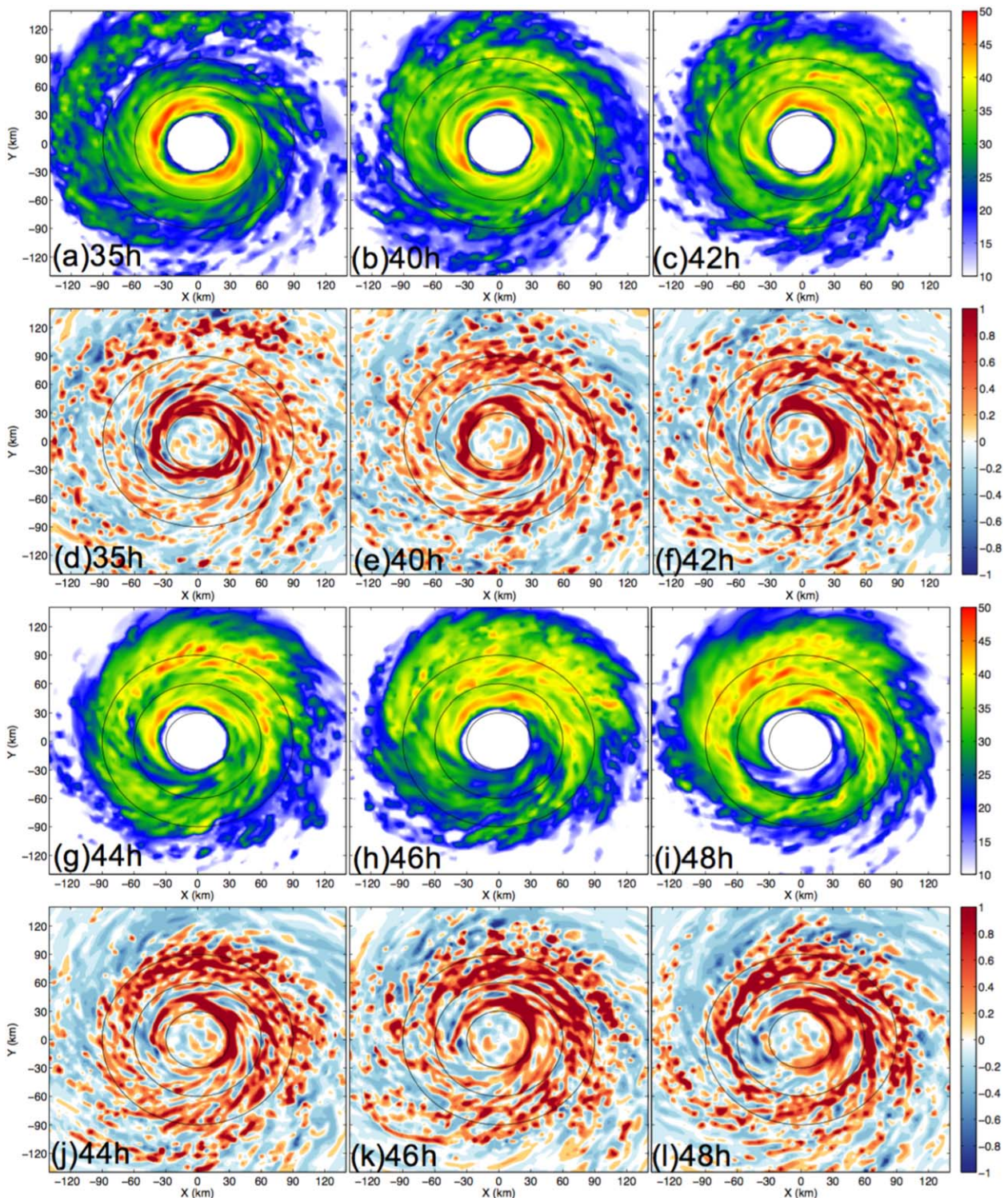
Figure 5. Horizontal plot for FullERC. (a–c and g–i) dBZ at 3 km; (d–f and j–l) vertical wind at 3 km at 35, 40, 42, 44, 46, and 48 h. Range rings are shown at radii of 30, 60, and 90 km.

convection are observed at around 70–100 km radius with a clear separation from the primary eyewall convection (Figures 4f, 5b, and 5e). Although the updrafts and reflectivity remain the strongest in the primary eyewall, there is apparent development of secondary maximum of reflectivity in the plane view (Figure 5c) from 60 to 90 km radius. This strong secondary maximum is also seen in the vertical wind field, most of

which are on the downshear-left side between 60 and 90 km radius due to downshear left preference of the convection under the westerly vertical wind shear [*Black et al.*, 2002; *Chen et al.*, 2006]. The primary eyewall updraft weakens considerably in the southwest-to-south quadrant of the TC during the following few hours. By 48 h, the secondary eyewall forms a complete circle which also has a stronger updraft in nearly all quadrants by this time while the original primary eyewall is undergoing its rapid demise losing the local maximum in reflectivity in almost all sides (though still visible in the updraft) except for in the northeast quadrant that begins to merge with the developing secondary eyewall (Figures 5i and 5l), indicating the near completion of the ERC in these ensemble members and their composite. It is interesting that the breakdown of the primary eyewall begins in its southern part, which suggests that, the spiral rainband with vigorous convection at the northern part might act as an upstream barrier to create hostile conditions to the inner eyewall further downstream. The primary eyewall, in the meantime, can be directly weakened in the southwest quadrant by the environmental shear. After the completion of ERC, the TC has a larger eye and a thicker eyewall (Figure 4f).

Figure 6 shows the composite vertical cross sections of the secondary circulations (indicated by the azimuthally averaged radial wind and vertical velocity), diabatic heating rate, and tangential wind every 5 h during a ~1 day period prior to the completion of ERC. A fairly typical secondary circulation exists from 20 to 35 h that features a rather near-uniform inflow in the boundary layer before reaching the ascent at the primary eyewall around 30 km radius (Figure 6a). The strongest outflow with over 8 m s^{-1} radial outward wind is located near the tropopause level (at ~12 km) while just above the boundary layer (~1.5 km) there is a secondary maximum of radial outflow likely as a response to the overshooting of the boundary layer inflow (as noted in many previous studies, e.g., *Kepert and Wang* [2001]). Despite the predominance of the primary eyewall updraft, the secondary circulation in the meantime, also features an azimuthally averaged local maximum of much weaker updraft centered at the 150 km radius and 9 km altitude (Figures 6a–6c). There is also a weak mid-to-upper tropospheric inflow just outside of the secondary updraft center (and maybe a hint of another even weaker inflow center in between the primary and secondary updraft centers at this high altitude). Consistent with past studies of *Fang and Zhang* [2012] and *Rozoff et al.* [2012], this secondary updraft maximum at high levels is likely attributable to the stratiform processes in the developing outer rainbands whose downward and inward building eventually leads to the formation of the secondary eyewall (Figures 6g–6i). A secondary maximum in the outflow above the inflow layer is observed near 60 km, and will be discussed further in section 6. The outer convection gradually connects with this secondary outflow maximum (Figures 6b, 6c, 6g, and 6h) and forms the secondary eyewall. A clear coexistence of the primary and secondary eyewall is seen at 40 and 45 h (Figures 6h and 6i) during which time the surface convergence center of the radial wind shifts to maximize from the original primary eyewall to the developing secondary eyewall as part of the ERC. The coexistence of the two eyewalls is further supported by the corresponding tangential wind field and diabatic heating (Figures 6d–6f and 6j–6l); the 30 m s^{-1} tangential wind contour starts to bend toward the secondary updraft from 20 h (Figure 6e) while the increasing diabatic heating outside the primary eyewall are collocated with the strengthening secondary updraft.

The importance of this secondary updraft center in the SEF can be further quantified through the tendency of the tangential wind in the radius-height plane: there is a clear positive tendency center of tangential wind collocated with this secondary updraft center at the radii between 120 and 150 km (and above the boundary layer) from 15 to 20 h (Figure 7a). Over the next few hours (20–25 h), this secondary tangential wind tendency maximum quickly descends to maximize at around 3 km height and 120 km radius extending to the boundary layer while the tangential wind tendency in the boundary layer under the primary eyewall becomes less strong (Figure 7b). This local tangential wind tendency maximum associated with the incipient secondary eyewall further builds just above the boundary layer (2 km) in a rather broad radius (from 80 to 150 km) from 25 to 30 h which begins to exceed the tangential wind tendency maximum in the primary eyewall (Figure 7c). Over the subsequent 5 h (30–35 h), the primary eyewall begins to weaken (with a negative overall tangential wind tendency throughout the column) with a concomitant reduction of the inflow and the consequent reduction of the convective heating by the developing secondary eyewall which now has maximum positive tangential wind tendency throughout the vertical column (Figure 7d). A similar trend continues and magnifies from 35 to 50 h (Figures 7f–7i), the completion time of the ERC, by which time the tangential tendency maximum near the surface is located just at the 50 km radius while the primary eyewall rapidly demises inside (Figure 7i). The integrated effect of the tangential wind tendency can also be seen in the evolution of corresponding total tangential wind field.
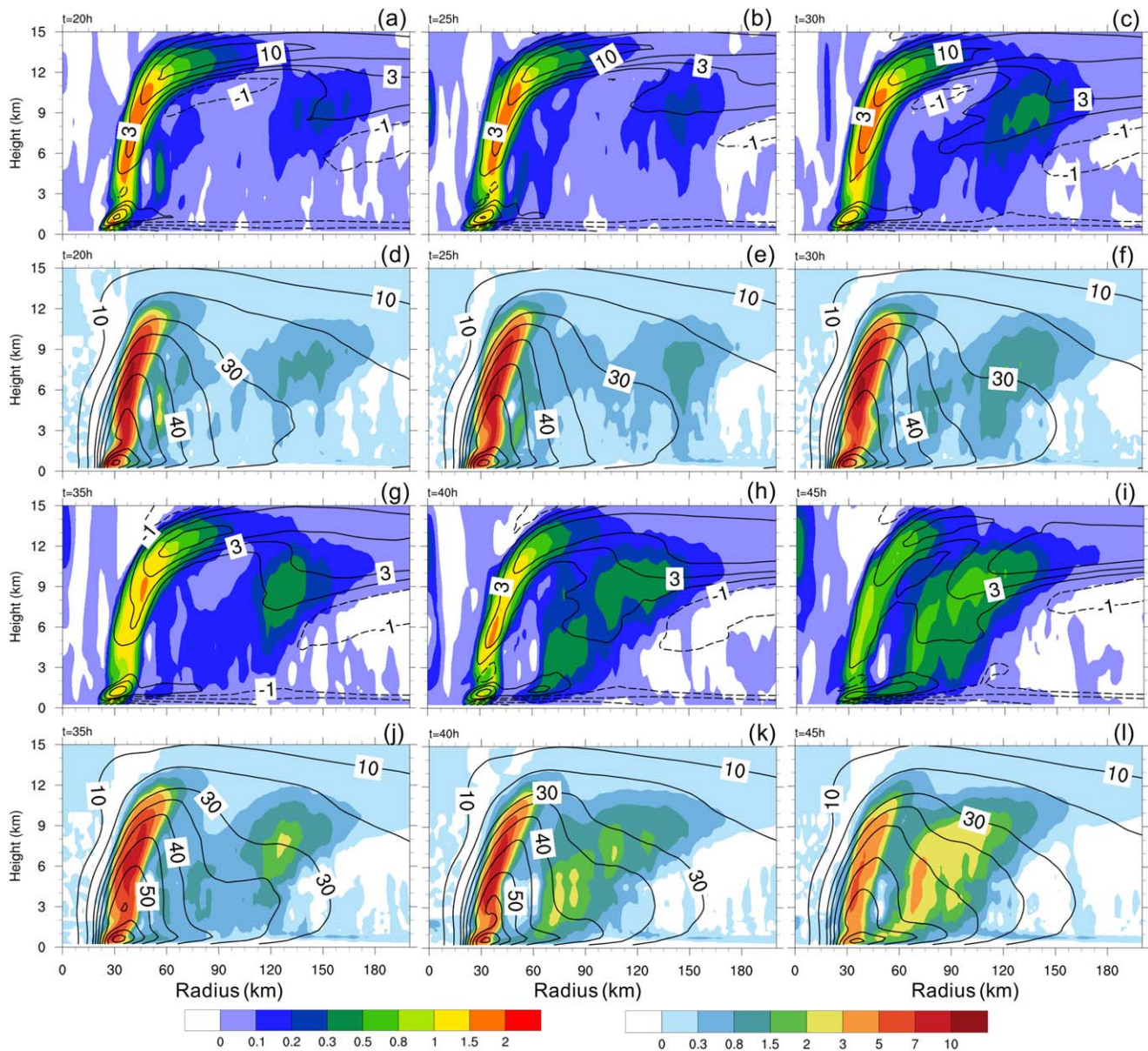
Figure 6. Vertical cross section of azimuthally averaged radial flow (solid line for outflow, dash line for inflow, m s^{-1}) and vertical velocity (shading, m s^{-1}) for FullERC at (a) 20 h; (b) 25 h; (c) 30 h; (g) 35 h; (h) 40 h; (i) 45 h. Vertical cross section of azimuthally averaged tangential wind (contour, m s^{-1}) and diabatic heating rate (shading, 10^{-3} K s^{-1}) for FullERC at (d) 20 h; (e) 25 h; (f) 30 h; (j) 35 h; (k) 40 h; (l) 45 h.

Figures 8a–8c and 8g–8i show the radius-height distributions of azimuthally averaged potential vorticity (PV) and equivalent potential temperature (θ_e) while Figures 8d–8f and 8j–8l present the radial gradient of θ_e along with the secondary circulation. From 25 h, we can see a weak secondary PV maximum in the midle-vel just outside the 60 km radius between 5 and 6 km height (outside of the primary core maximum) which gradually strengthens (Figures 8a–8c). A distinct midlevel PV center outside of the core vortex was estab-lished at 35–40 h maximized at 6 km and expands downward (Figures 8b and 8c). By 45 h, this outside PV maximum starts to merge with the strongest inner-core PV from the low levels (Figure 8g). The low-level θ_e (especially 345 K contour) from 35 to 45 h (Figures 8b, 8c, and 8g) bends to increase the frontal-like θ_e gradi-ent (Figures 8e, 8f, and 8j) between 60 and 90 km in the upper boundary layer, which is also observed in *Fang and Zhang* [2012]. This secondary maximum of a frontal-like θ_e gradient is collocated under the enhanced PV maximum in the middle level at a distance outside of the primary eyewall (Figures 8b, 8c, 8e, and 8f). Likely related to the stratiform processes discussed in *Fang and Zhang* [2012], the enhanced PV in
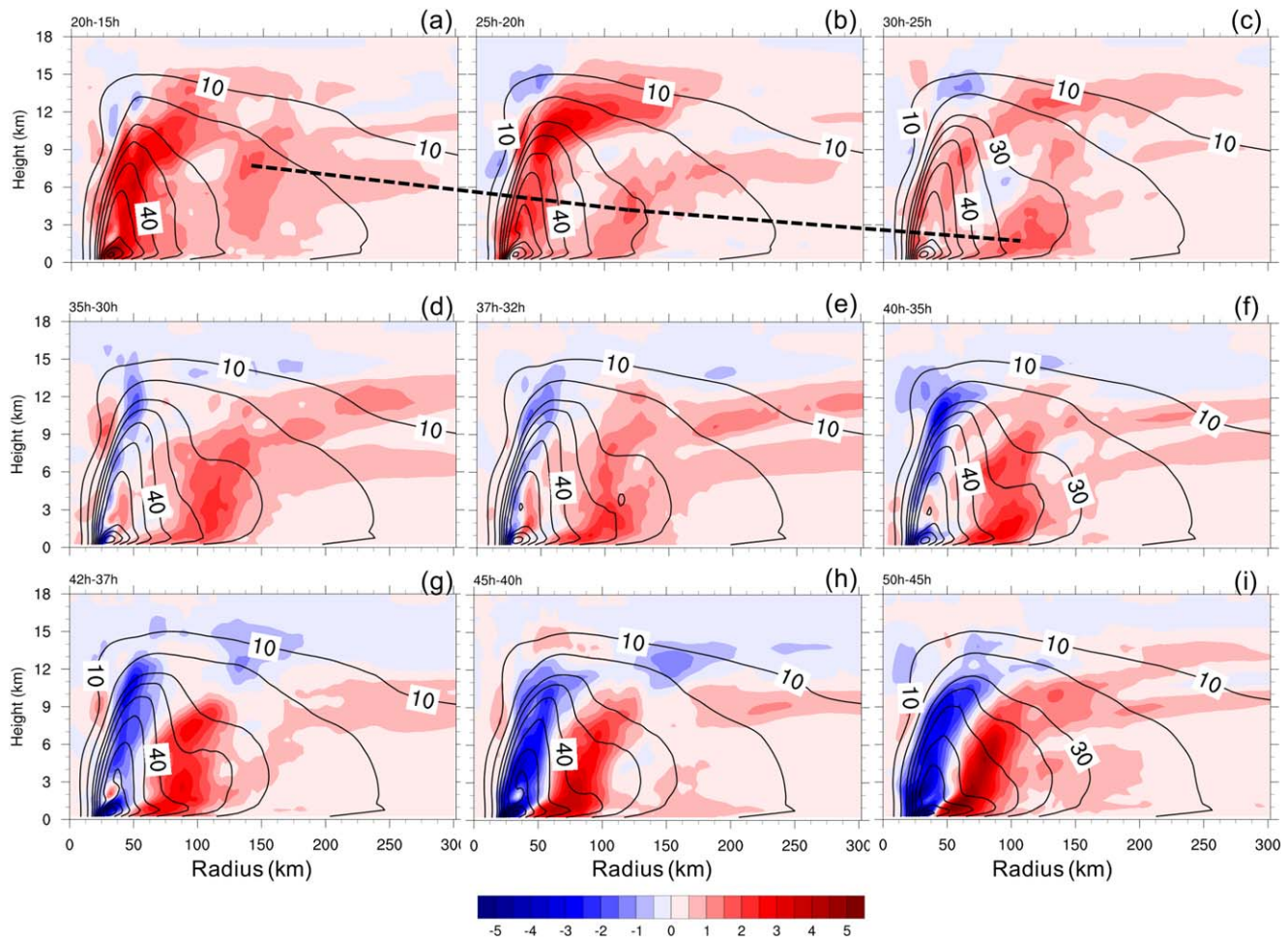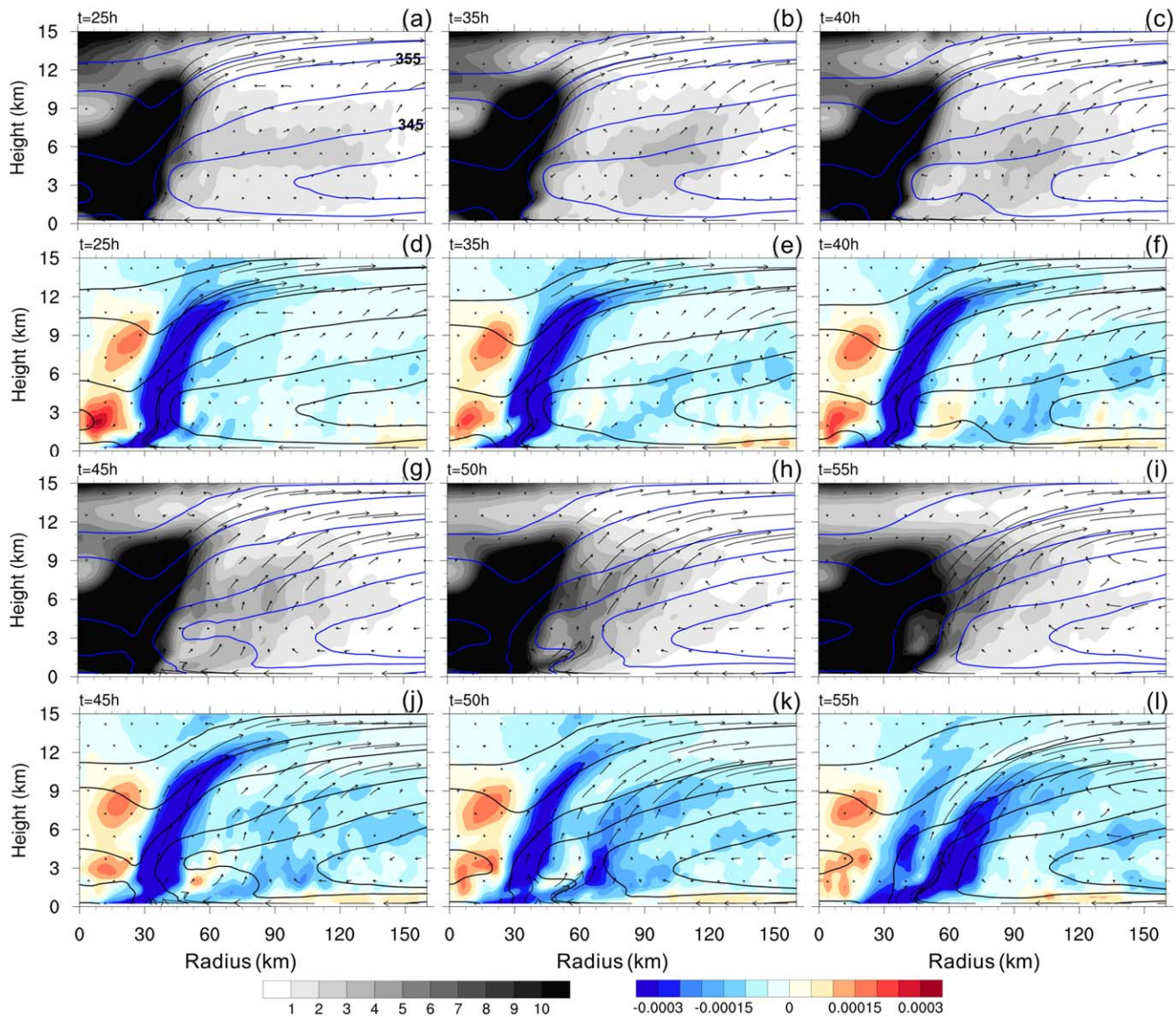
Figure 7. Azimuthally averaged tangential wind tendency (dv/dt, m s^{-2}, 5 h summation) of FullERC for (a) 20–15 h; (b) 25–20 h; (c) 30–25 h; (d) 35–30 h; (e) 37–32 h; (f) 40–35 h; (g) 42–37 h; (h) 45–40 h; (i) 50–45 h. Contour is the tangential wind at each earlier time. The dash line tracks the secondary tendency maximum.

the inner and outer eyewall merges gradually from the lower to the upper level during and after the eyewall replacement which eventually forms a wide enhanced PV region. Comparing Figures 8a and 8i, we can see that after SEF, the large PV area extends to about 60 km, consistent with the change in the eye size.

## 5. Composite Analysis of Five Selected Members With Partial SEF/ERC

To further understand the dynamics and predictability of the SEF/ERC processes discussed in the previous section, we also select another five members (S_MEM7, S_MEM8, J_MEM1, J_MEM4, and J_MEM11) that display some characteristics of eyewall replacement but fail to establish a persistent, completed secondary eyewall in comparison to the members in the FullERC composite. Figure 9 shows a zoomed-in view of these five elected members that either do not have a clear secondary updraft maximum outside of the primary updraft and/or do not have clear moat that separates the primary and secondary eyewalls (and thus are termed as partial SEF/ERC or PartERC for the composite). As for the FullERC composite, these PartERC members and composite are shown from around 40 h before the appearance of a partial secondary eyewall and 20 h after the expansion of the eye for a total timespan of 70 h (denoted by the dashed box in Figures 2 and 3). It is worth noting first that the primary updrafts in the FullERC members (Figure 4) are on average stronger than those in the PartERC members (Figure 9) at the beginning of the composite (with the completion of RI) but this is likely due to difference in the length of rapid intensification time before the start of SEF/ERC.

Figure 8. Vertical cross section of azimuthally averaged potential vorticity (shading, PVU) and secondary circulation (curly vectors, vertical wind is multiplied by 10, m s^{-1}) and equivalent potential temperature (blue contours, K) for FullERC at (a) 25 h; (b) 35 h; (c) 40 h; (g) 45 h; (h) 50 h; (i) 55 h. Vertical cross section of azimuthally averaged equivalent potential temperature gradient (shading, K m^{-1}) along radius direction and secondary circulation (curly vectors, vertical wind is multiplied by 10, m s^{-1}) and equivalent potential temperature (black contours, K) for FullERC at (d) 25 h; (e) 35 h; (f) 40 h; (j) 45 h; (k) 50 h; (l) 55 h. Numbers in Figure 8a indicate the equivalent potential temperature contours of 355 and 345 K.

Figure 10 shows the horizontal map view of simulated reflectivity and vertical velocity fields at 3 km height at selected times for the PartERC composite. In comparison to FullERC in Figure 5, it is apparent that the PartERC composite has less vigorous convective activity outside of the primary eyewall and that the developing outer rainbands are less symmetric. While the PartERC composite also tries to develop a secondary updraft maximum outside of the primary eyewall (at the 60 km radius around 40 h; Figures 10b and 10c), this secondary maximum quickly merges with the primary eyewall at around 42 h (Figures 10c and 10f). But the expansion of eye is not seen until 50 h (not shown).

Figure 11 shows the vertical cross sections of the composite secondary circulations, azimuthally averaged tangential wind and diabatic heating prior to the completion of the partial ERC. There also exists a secondary updraft maximum between the heights of 9–12 km and radii of 90–150 km in the PartERC composite (Figures 11a and 11b) that is similar to FullERC (Figures 6a and 6b) but it is considerably weaker which struggles to connect with the boundary layer updraft to form a coherent secondary eyewall. Meanwhile, another area of enhanced updraft just outside the primary eyewall at around the 45 km radius from 35 h onward
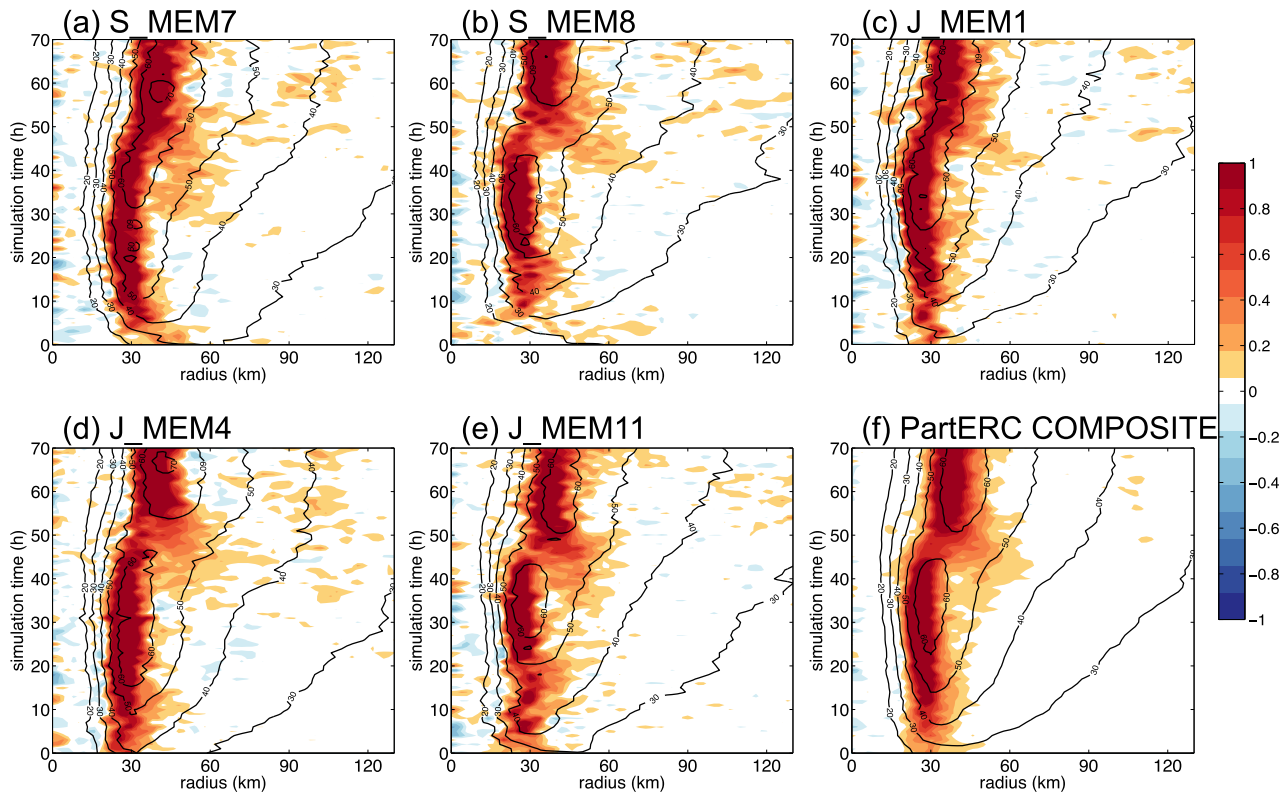
Figure 9. Vertical (shading, m/s) and tangential (contour, m/s) wind at 1 km for (a) member 7 on Stampede (S_MEM7); (b) member 8 on Stampede (S_MEM8); (c) member 1 on Jet (J_MEM1); (d) member 4 on Jet (J_MEM4); (e) member 11 on Jet (J_MEM11). (f) Vertical and tangential wind composite of five ensembles (hereafter PartERCs) at 1 km. The time is rescaled to match the start time of eye expansion at 50 h.

(Figures 11a–11c and 11g–11i) may have hindered the moat formation at this distance but instead serves to bridge the two eyewalls which makes it unable to completing a full replacement cycle in the FullERC composite (Figure 11 versus Figure 6).

We also examine the tendencies of tangential wind at selected times for the PartERC (Figure 12) in comparison to those in FullERC. Likely due to slightly weaker initial intensity at the start of the composite, the strengthening (and expansion) of the primary eyewall tangential circulation persists somewhat longer in PartERC (Figures 12a–12e) than in the FullERC composite (Figures 7a–7c) while the downward development of the positive tendency associated with the incipient/future secondary eyewall is less evident in PartERC (Figures 12a–12c versus Figures 7a–7c). Nevertheless, the overall evolution of the tangential wind tendency is strikingly similar between the FullERC and PartERC (Figure 12 versus Figure 7) suggesting the difference between the partial and full ERC is subtle rather than distinct, whose predictability is likely subject to the randomness in convection to form the difference in extent and strength of outer rainbands before or during the eyewall replacement process.

6. SEF and ERC: Nonlinear Boundary Layer Diagnostics on the Role of Balanced Dynamics

The axisymmetric secondary circulation in a hurricane is usually understood as being forced by a combination of momentum forcing and diabatic heating. To understand the contribution of frictional forcing within the boundary layer to the secondary circulation, we need to diagnose the response of the vortex to friction. As discussed in section 2.2, we use a nonlinear version of the diagnostic tropical cyclone boundary layer model developed by *Kepert and Wang* [2001], with modifications as described in *Kepert* [2012, 2013] and *Kepert and Nolan* [2014]. Hereafter we refer to this as the KW01 model.
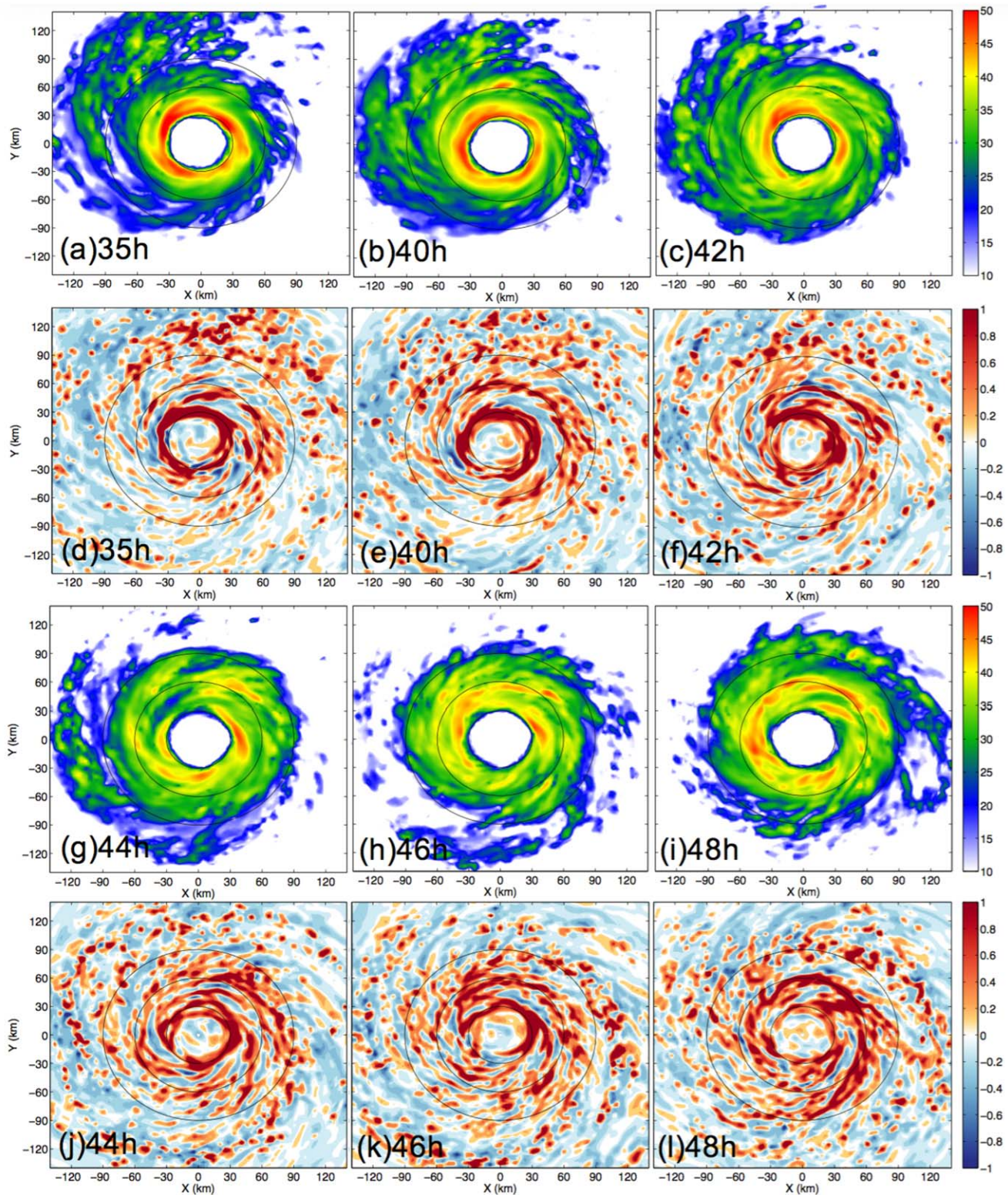
Figure 10. Horizontal plot for PartERC. (a–c and g–i) dBZ at 3 km; (d–f and j–l) vertical wind at 3 km at 35, 40, 42, 44, 46, and 48 h. Range rings are shown at radii of 30, 60, and 90 km.

6.1. Balanced Diagnosis From the BL Model

Figure 13 shows Hovmöller diagrams of the diagnosed boundary layer flow from the KW01 model and the WRF FullERC composite. The diagnosed radial and azimuthal flow (Figures 13b and 13d) each show a very
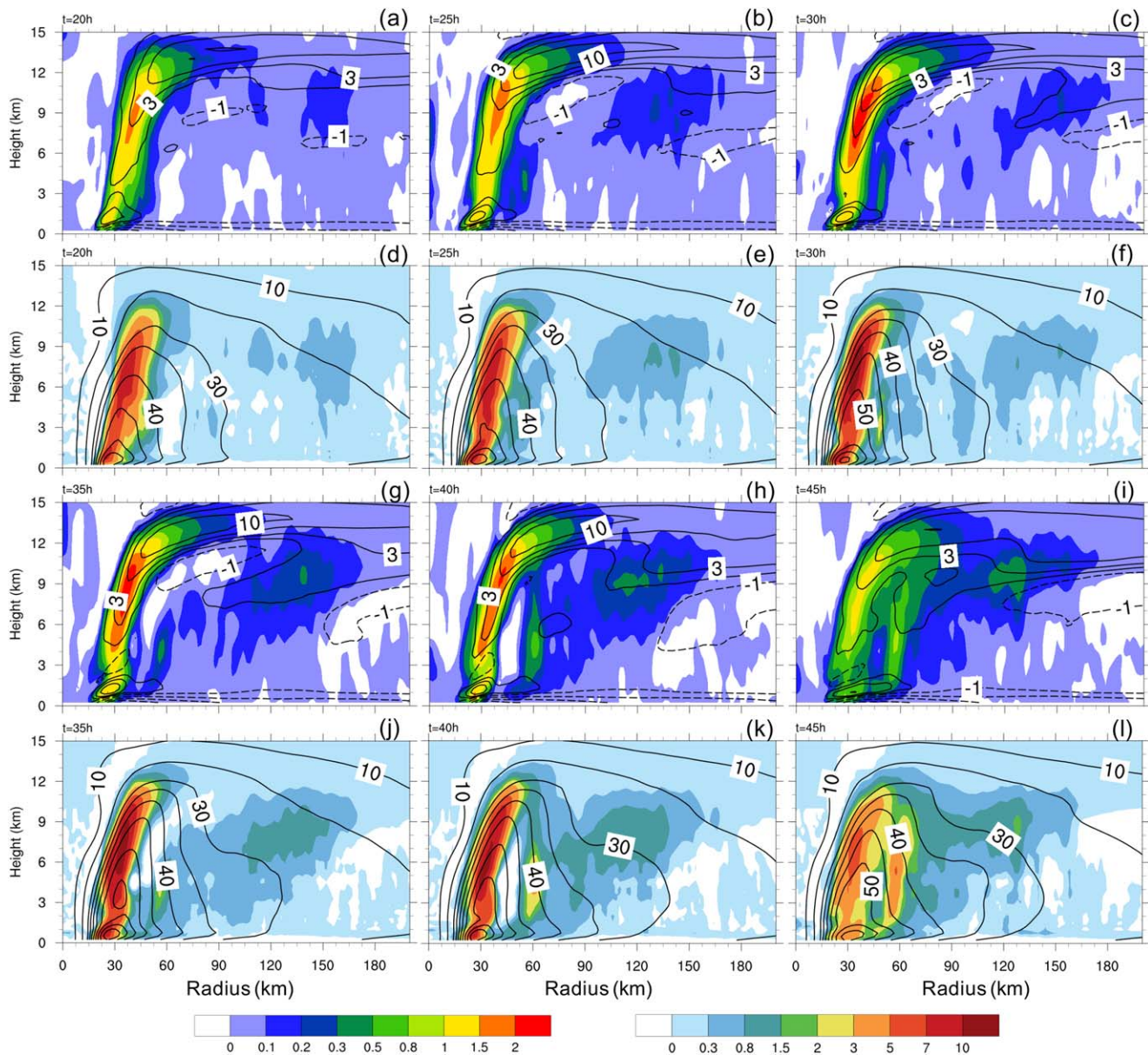
Figure 11. Vertical cross section of azimuthally averaged radial flow (solid line for outflow, dash line for inflow, m s^{-1}) and vertical velocity (shading, m s^{-1}) for PartERC at (a) 20 h; (b) 25 h; (c) 30 h; (g) 35 h; (h) 40 h; (i) 45 h. Vertical cross section of azimuthally averaged tangential wind (contour, m s^{-1}) and diabatic heating rate (shading, 10^{-3} K s^{-1}) for PartERC at (d) 20 h; (e) 25 h; (f) 30 h; (j) 35 h; (k) 40 h; (l) 45 h.

similar evolution to the WRF ensemble mean (Figures 13a and 13c), with a steady outward expansion of the inflow and azimuthal wind, the formation of an inner maximum associated with the primary eyewall, and its replacement with an outer maximum. The diagnosed inflow associated with the primary eyewall tends to be a little weak for the first 40 h, but is in better agreement for the secondary eyewall from 40 h, and the inflow relative minimum between the two eyewalls is a little stronger in the diagnostic model. The updraft sequences in the two models are similarly in close agreement, especially after about 30 h (Figures 13e and 13f). Some differences are apparent prior to that, where WRF has weaker ascent than the diagnostic model (including some minor patches of descent) between about 70 and 130 km radius, and stronger ascent further out. Possibly at this time, the frictional convergence is too weak to dominate over other influences on the development of convection, and/or the vortex is less symmetric. There are also differences at large radii later in the period, where the region of descent (blue shading) extends further inward in the diagnostic model. There are clear links between the evolution of the horizontal flow, the gradient wind and the
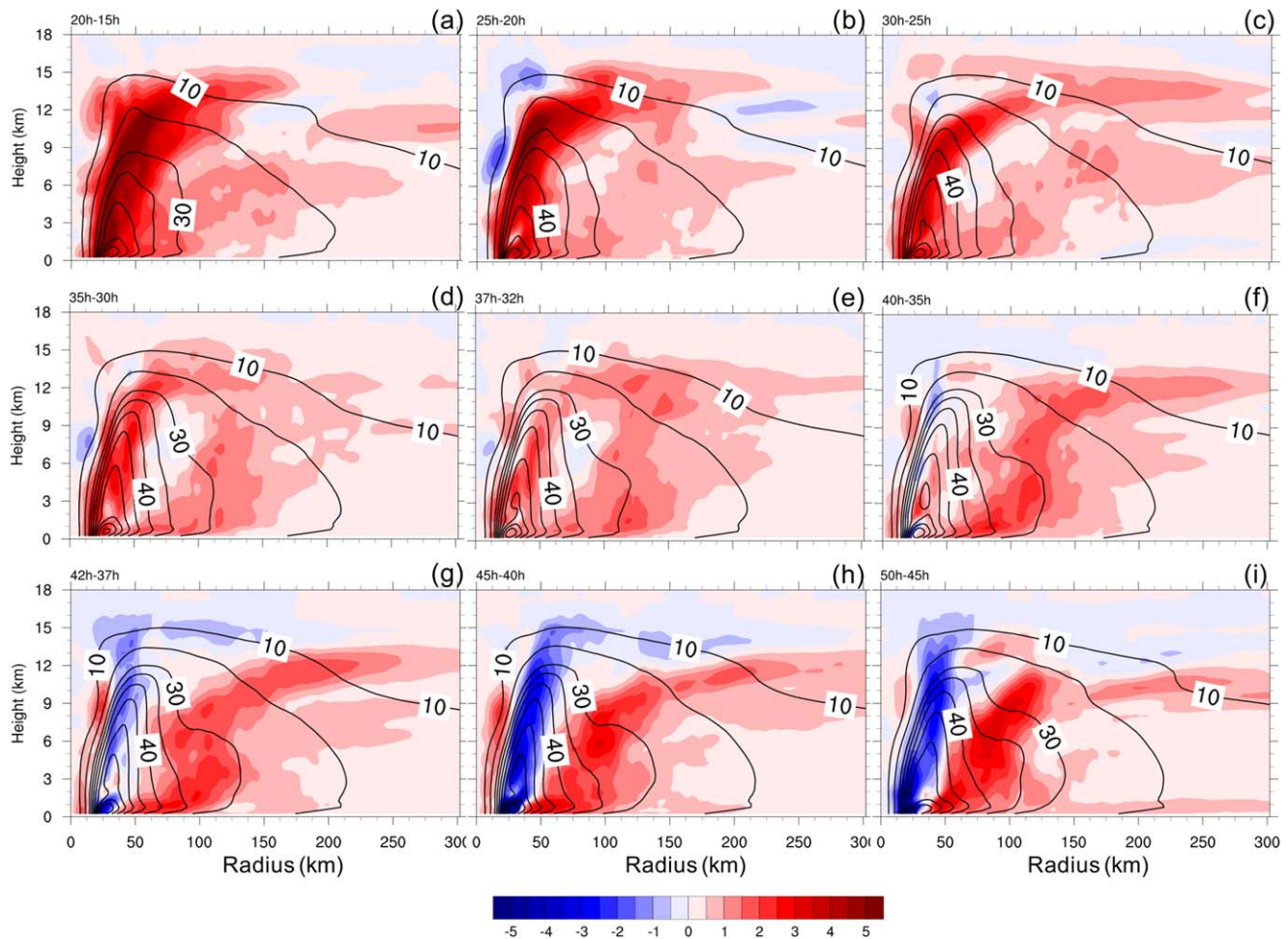
Figure 12. Azimuthally averaged tangential wind tendency (dv/dt, m s^{-2}, 5 h summation) of PartERC for (a) 20–15 h; (b) 25–20 h; (c) 30–25 h; (d) 35–30 h; (e) 37–32 h; (f) 40–35h; (g) 42–37 h; (h) 45–40 h; (i) 50–45 h. Contour is the tangential wind at each earlier time.

updraft. The links to the updraft are clearer if we examine the vertical vorticity of the gradient wind derived from the FullERC composite (Figure 13h), which reveals more of the finer-grained structure. In particular, the vorticity outside of about 60 km radius is roughly constant with radius out to the outer updraft region, up to about 30 h. After that, the vorticity in the 100–150 km band tends to diminish with time, while a secondary vorticity maximum develops near 75 km radius around 35 h and subsequently contracts inward with the contracting secondary eyewall. In Figure 13, we saw that from about 30 h, the contracting and developing outer updraft was nearly collocated with the similarly contracting and intensifying vorticity feature. These results are thus both qualitatively and quantitatively consistent with the theory described by Kepert [2013].

Figure 14 shows radius-height cross sections of the azimuthal-mean horizontal flow at 5 h intervals starting from 34 h, a period which covers the decay of the inner eyewall and its replacement by the outer eyewall. The left column shows the ensemble-mean fields from WRF, while the right column shows the diagnosed flow from KW01. The slow outward expansion of the azimuthal flow and near-surface inflow are apparent. The outer inflow maximum first appears at 39 h in the diagnostic model, and a little later in WRF. The inner inflow maximum has disappeared by 49 h, in both models. Similarly, the azimuthal wind develops a marked lobe extending outward at 44 h, which develops into an outward shift of the wind maximum by 49 h. This outward redevelopment of the secondary wind maximum is accompanied by the strengthening of both the near-surface inflow and the outflow immediately aloft, with WRF and the diagnostic model again being in good agreement. The inflow is a little deeper in the diagnostic model, especially at large radii. The depth scale for the tropical cyclone boundary layer in a linearized model is $(2K/I)^{1/2}$ where K is the vertical
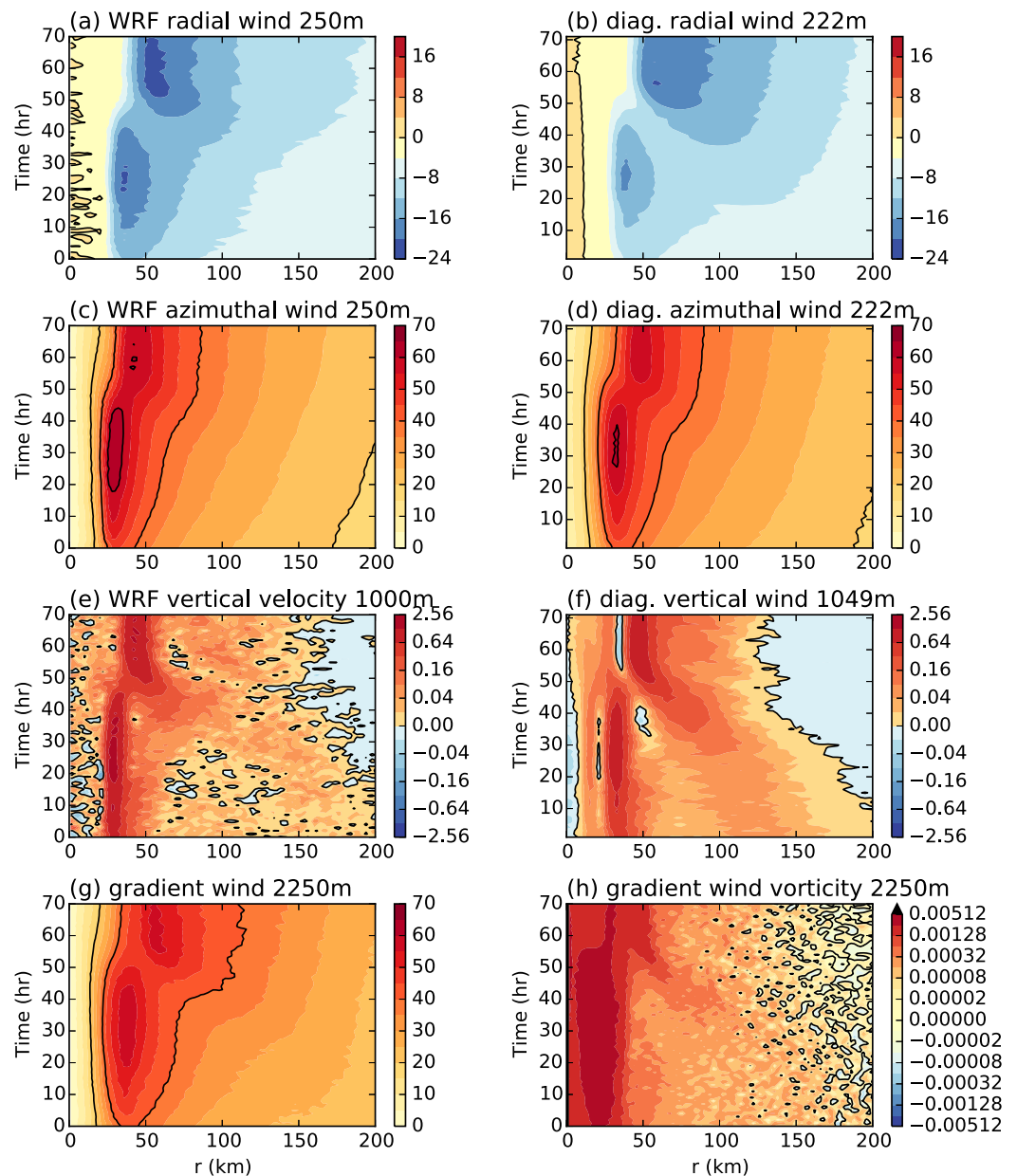
Figure 13. Hovmöller diagrams of (a and b) radial, (c and d) tangential, and (e and f) vertical flow, from (a, c, and e) WRF ensemble composite FullERC and (b, d, and f) the KW01 model. (g) The 2.25 km gradient wind from the WRF FullERC composite used to force the KW01 model, and (h) its relative vorticity.

diffusivity and "I" the inertial stability [*Kepert*, 2001] and so this may indicate that the parameterized diffusivity is too large in the KW01 model. Another slight systematic difference is that the diagnosed outflow near and above 1 km height associated with the eyewall is a little weaker in the diagnostic model, which also has a more radially continuous outflow layer.

Figure 15 shows radius-height sections of the vertical velocity for the same times as in Figure 14. Clearly the WRF field in Figure 15 (left) is substantially noisier than in the boundary layer model (right). At 34 h, the WRF fields (Figure 15a) show a marked outward-sloping primary eyewall, with fairly disorganized upward motion at larger radii. By 39 h (Figure 15c), this disorganized ascent has consolidated into a coherent updraft near 75 km radius, with greater outward slope than the primary eyewall. This updraft then migrates steadily inward while narrowing and intensifying, with the lower sections of the two updrafts merging at about 49 h (Figure 15g). The sequence in the boundary layer model is very similar, except that the updraft
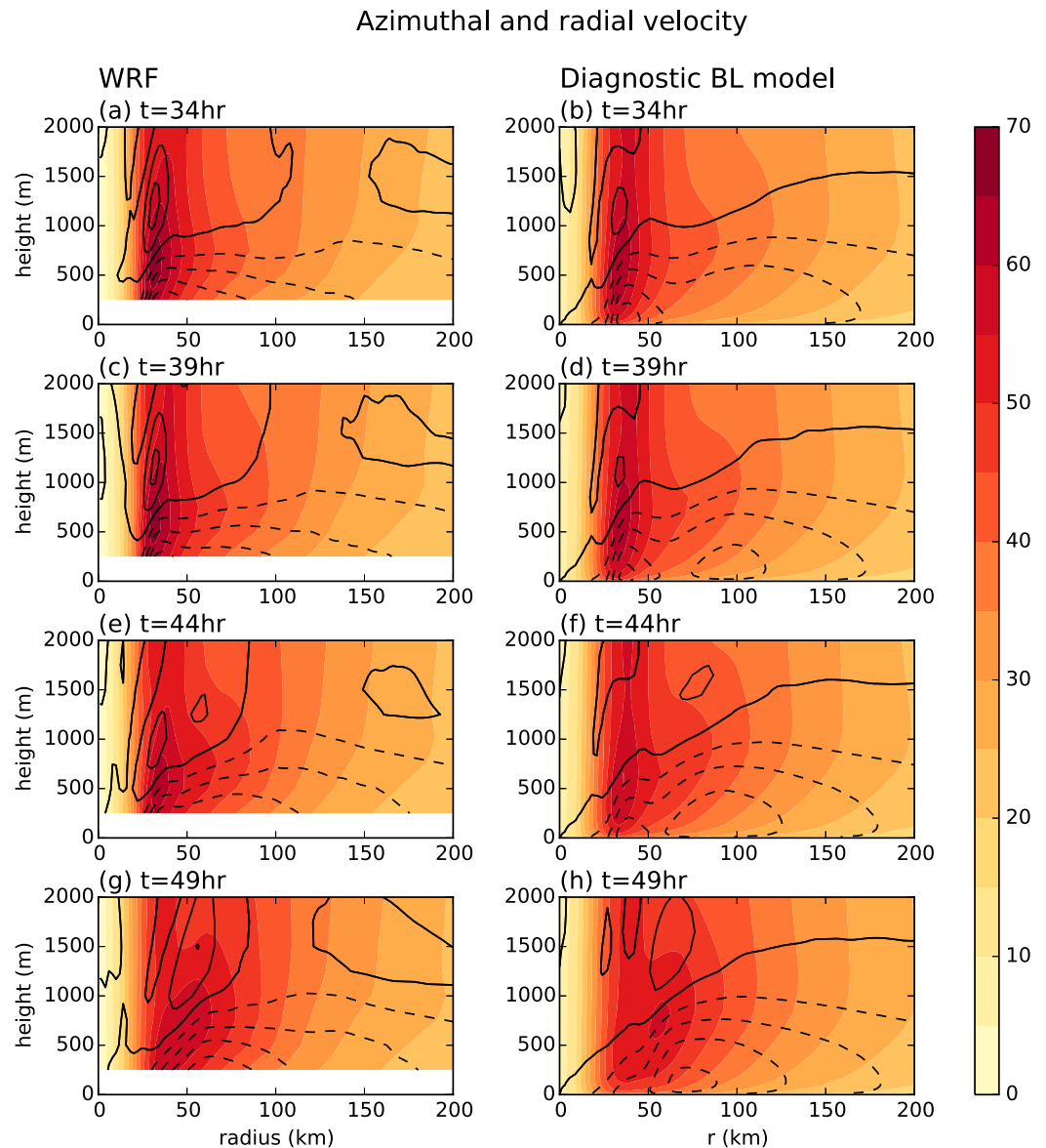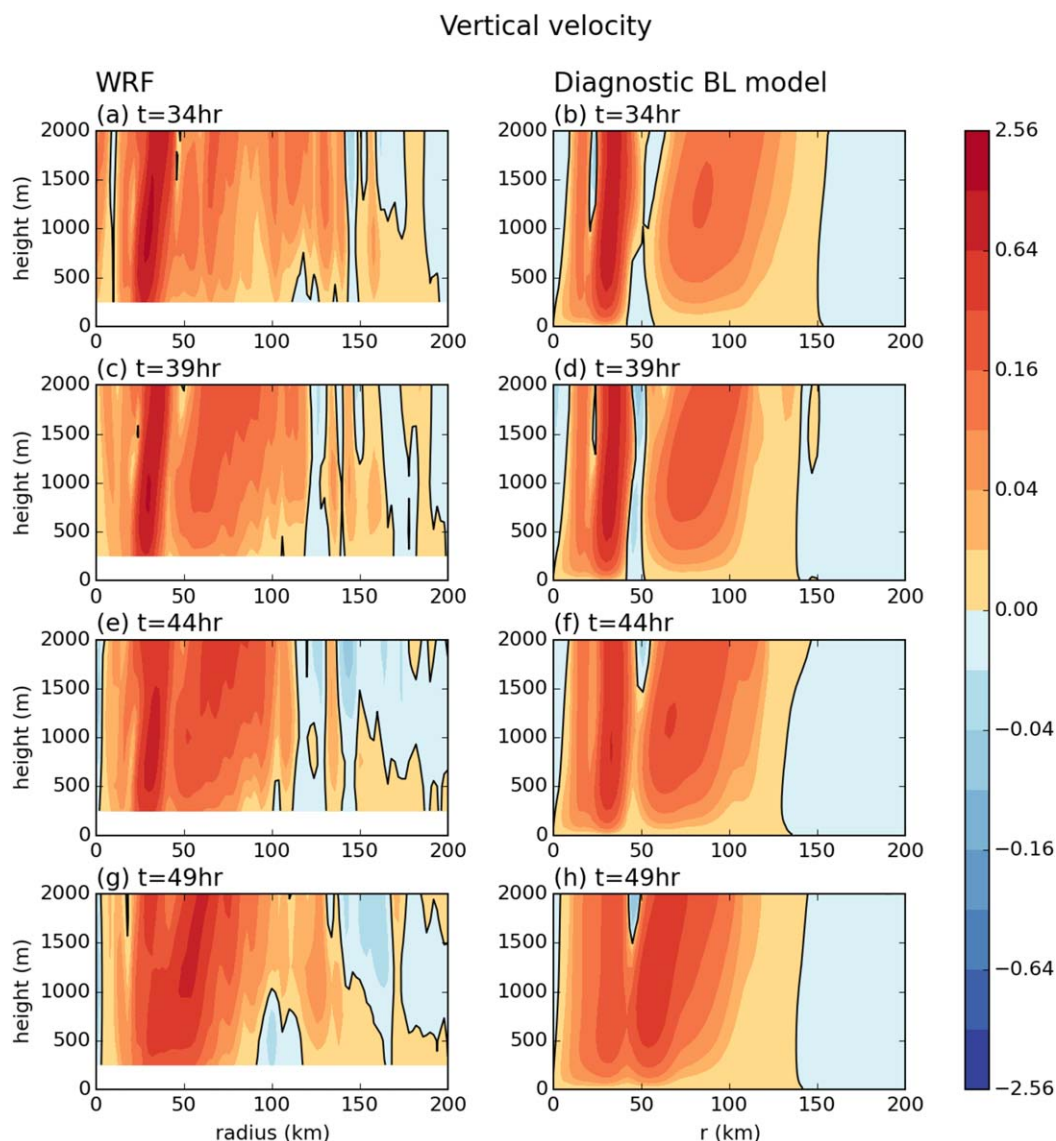
Figure 14. Radius-height sections of azimuthal wind (shading) and radial wind (contours). Contour interval is 5 m s^{-1}, negative contours dashed. At 5 h intervals from 34 to 49 h. Left column is WRF ensemble composite FullERC, right is from the KW01 diagnostic model.

is rather more coherent at 34 h (Figure 15b) and the main updrafts tend to be a little weaker, which is also shown in Figures 13e and 13f. There is also much clearer moat in the boundary layer model that separates the secondary updraft from the primary updraft with a descending region (Figure 15d). However, the location and outward slope of the secondary eyewall are in good agreement between the WRF results and boundary layer model results.

Similar analyses of the boundary layer flow were also done for the PartERC composite. Figure 16 is the same Hovmöller diagrams as Figure 13 but for PartERC. The most apparent difference between the PartERC and FullERC BL calculations is in the vertical wind and gradient wind vorticity. The secondary updraft and vorticity maxima are about half as strong and shorter lived in PartERC, but the relationship between these two features is similar. However, the boundary layer model tends to produce the secondary updraft at earlier time and clearly separated toward the primary updraft, similarly to FullERC. Figure 17 shows the same vertical cross section below 2 km height as Figure 14. The agreement between the two models is markedly weaker than in the FullERC case. In particular, the diagnostic model has a clear minimum in the updraft near r = 40 km up to hour 44, whereas WRF has reasonably strong ascent in the same location. The reasons for

Figure 15. Radius-height sections of vertical velocity. Nonzero contours are in geometric progression, at $\pm 0.02, \pm 0.04, \pm 0.08, \ldots \pm 2.56$ m s^{-1} and the zero contour is in black. At 5 h intervals from 34 to 49 h. Left column is WRF ensemble composite FullERC, right is from the KW01 diagnostic model.

this difference are unclear, but may be that the PartERC case is less symmetric at these times (Figure 10), so the assumption of axisymmetry in the diagnostic model is poorer. It may also be that the ascent in WRF at this radius is largely forced by convection rather than friction. In any event, the markedly weaker outer eyewall frictional updraft diagnosed in the PartERC case would presumably have far less influence on the distribution and intensity of convection than in the FullERC case.

6.2. Discussion

The good agreement between the WRF ensemble-mean and the diagnostic boundary layer model for the FullERC and PartERC demonstrates that the azimuthal-mean flow in the lowest 2 km of the simulation is largely determined by the processes included in the diagnostic boundary layer model. The boundary layer model neglects moist processes, which explains some differences between the WRF and BLM simulations. The greater fine-scale structure in the WRF simulation is on the space scale of ~10 km and time scale of less than an hour, and is therefore likely due to convection. The tendency for stronger updrafts and slightly stronger inflow in WRF can probably be attributed to that the secondary circulation that is forced by latent heat release, which is consistent with the study by *Stern et al.* [2015]. They diagnosed the inflow difference
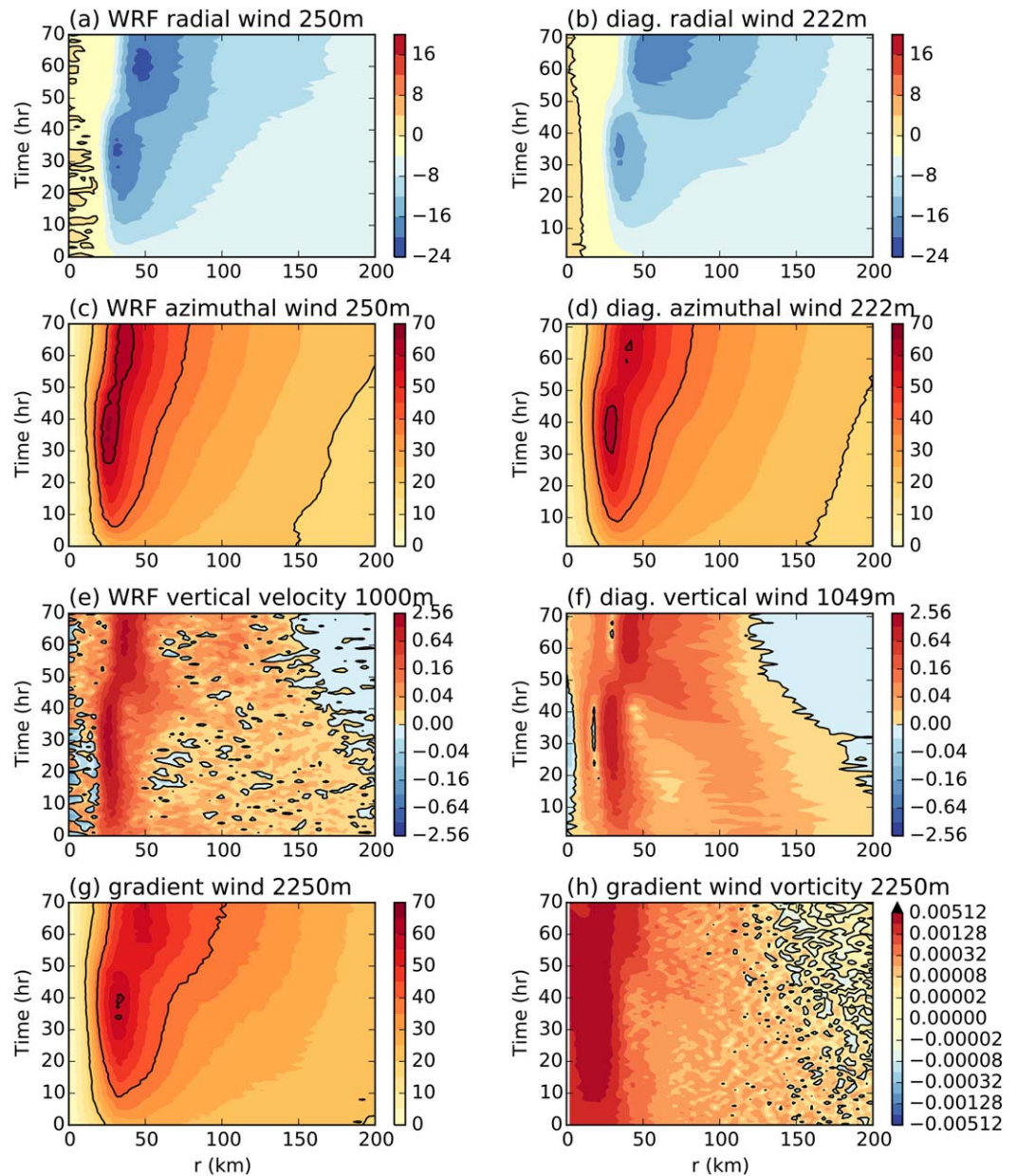
Figure 16. Hovmöller diagrams of (a and b) radial, (c and d) tangential, and (e and f) vertical flow, from (a, c, and e) WRF ensemble composite PartERC and (b, d, f) the KW01 model. (g) The 2.25 km gradient wind from the WRF PartERC composite used to force the KW01 model, and (h) its relative vorticity.

between a WRF simulation and the 3DVPAS model [*Nolan and Montgomery*, 2002; *Nolan and Grasso*, 2003] in the range of 1–3 m s^{-1}, which is similar to the difference in the inflow in the two models apparent in Figure 15.

Apart from these differences, we see good agreement between the actual azimuthal-mean ensemble-mean flow and that derived from the boundary layer model. Recall that the only information that the boundary layer model receives from WRF is the azimuthal-mean ensemble-mean pressure field at 2.25 km height, as represented by the gradient wind. The boundary layer flow is diagnosed as the steady state response to this mass field. Hence the boundary layer in the WRF simulation can, to good approximation, be regarded as being "slaved" to the parent vortex, in the sense that the boundary layer flow is close to the equilibrium response to pressure field of the parent vortex. The conclusion is supported by theory. *Eliassen and Lystad* [1977] showed via a scaling argument that the time scale for diffusive adjustment of the tropical cyclone
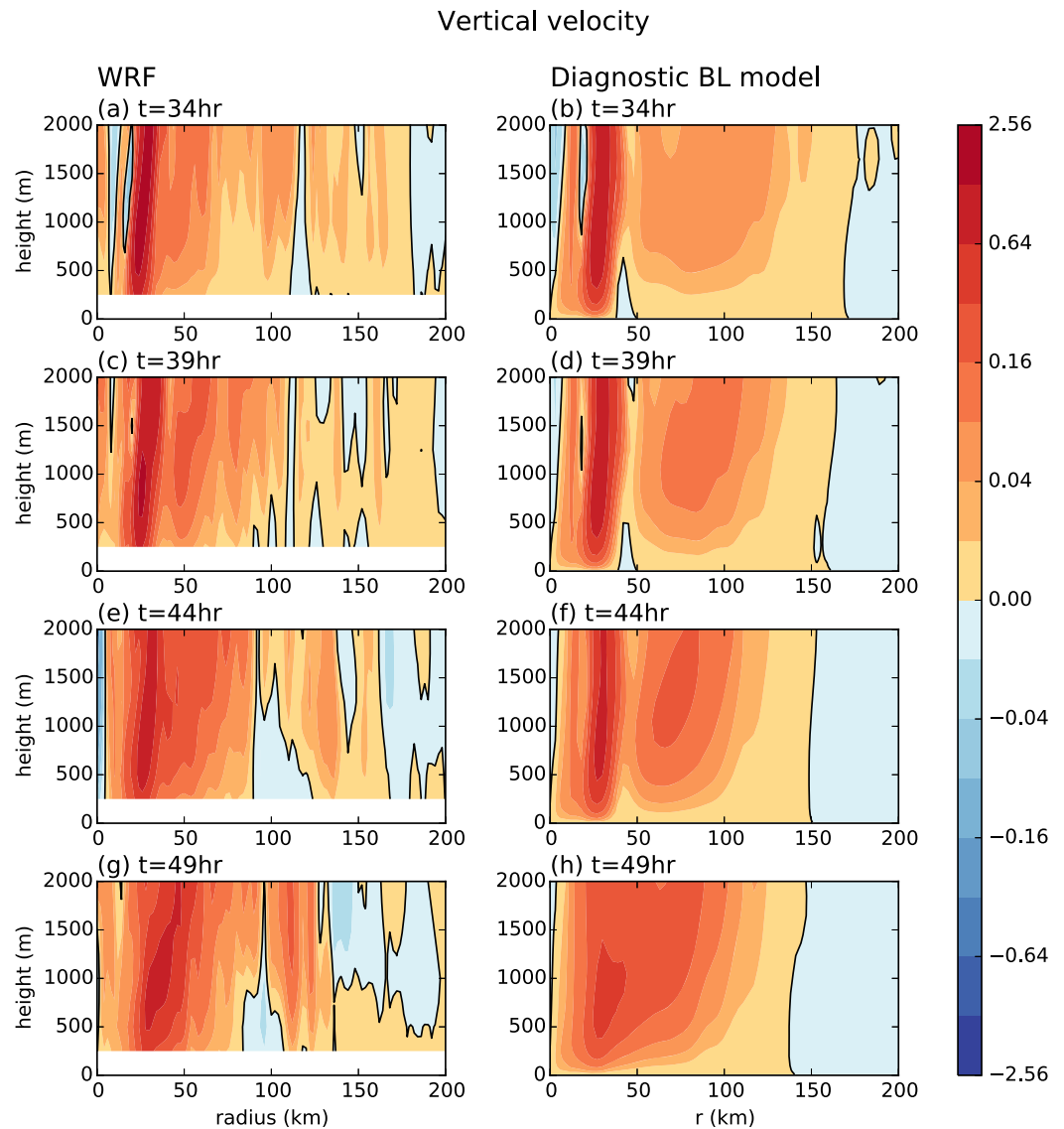
Figure 17. Radius-height sections of vertical velocity. Nonzero contours are in geometric progression, at $\pm 0.02, \pm 0.04, \pm 0.08, \ldots \pm 2.56$ m s^{-1} and the zero contour is in black. At 5 h intervals from 34–49 h. Left column is WRF ensemble composite PartERC, right is from the KW01 diagnostic model.

boundary layer to equilibrium with the parent vortex is I^{-1} where I is the inertial stability. *Kepert and Nolan* [2014] noted that this time scale is substantially shorter than that over which tropical cyclones undergo significant structure or intensity change, within a few times the RMW of the cyclone center. They concluded that because the boundary layer in this region adjusts more rapidly than the parent vortex, it could be approximated as being always close to equilibrium with the parent vortex. In other words, the evolution of the boundary layer flow is well represented as the response to the evolving mass field, with the time-tendency terms within the BL being largely irrelevant.

These results are also consistent with *Kepert* [2013] analysis of the boundary layer flow associated with both developing, and fully formed, outer eyewalls. He showed that in a cyclone with two wind maxima of similar strength, the outer one produces a much stronger frictional updraft. Even if the outer maximum is reduced to a small bump in the gradient wind profile, it can still produce an appreciable updraft. He explained these results using an analytical equation for the updraft obtained from the linearized model of *Kepert and Wang* [2001], showing that it was the presence of a locally stronger radial gradient of the vorticity of the gradient wind that produced the updraft. Such gradients produce larger updrafts at large radii than smaller, because

(a) Stage I: redevelopment and expansion of remnant shear-induced outer rainbands after completion of primary vortex alignment and rapid intensification;

(b) Stage II: expansion of outer tangential wind and change of inertial stability through developing outer convection, emergence of discrete outer updraft from boundary layer processes and axisymmetrization of outer rainbands;

(c) Stage III: formation and development of the secondary eyewall through extension of the outer updraft to the boundary layer and positive feedback between boundary layer processes;

(d) Stage IV: completion of the eyewall replacement cycle with weakening of the primary eyewall and strengthening of the secondary eyewall.

Figure 18. A multistage schematic diagram of secondary eyewall formation in sheared tropical cyclones.

they are in an environment of lower vorticity at large radii. The relationship between this vorticity field and the frictional updraft is consistent with the theory of *Kepert* [2013] and the analysis of a WRF simulation by *Kepert and Nolan* [2014]. In particular, the secondary eyewall's updraft tends to be roughly collocated with the development of a local secondary maximum of the gradient vorticity in both FullERC and PartERC, though the boundary layer model tends to simulate the two eyewall updrafts slightly further away from each other than the separation distance simulated in the WRF composites.

7. Concluding Remarks

This study examines the predictability and dynamics of tropical cyclone (TC) secondary eyewall formation (SEF) and intensity changes under moderate environmental vertical wind shear through a series of cloud-resolving ensemble simulations.

Consistent with what have been discussed in *Zhang and Tao* [2013] and *Tao and Zhang* [2015], in the presence of environmental shear, the initial random perturbations will ultimately change the timing of rapid intensification, and subsequent eyewall replacement cycles. Moreover, the same level of intensity divergence can also be found between experiments with exactly the same initial conditions under the same environment but are performed on different computer clusters, which is reminiscent of the "butterfly effect" that led to the development of the chaos theory half a century ago.

Through composite analyses from five ensembles with similar ERC and another five with only partial ERC, and diagnostics with a nonlinear boundary layer (BL) model, we have identified the four stages in the SEF process as illustrated in the schematic diagrams of Figure 18. Stage I begins with the redevelopment and expansion of the remnant shear-induced outer rainbands after the completion of the primary vortex alignment and rapid intensification (Figure 18a). In Stage II, the developing outer rainband convection leads to the expansion of outer tangential wind field and the change of inertial stability while a discrete outer

updraft begins to emerge from axisymmetrization of outer rainbands along with boundary layer processes (Figure 18b). The moderate environmental shear is primarily responsible for the development of the outer raindband whose associated enhanced latent heating leads to the expansion of the outer wind fields and the inertial stability changes [e.g., *Rozoff et al.*, 2012]. In the cases where SEF occurs, this wind field expansion contains a distinct secondary local maximum in the gradient wind vorticity, which leads to a secondary frictional updraft maximum through the boundary layer dynamics. In Stage III the downward development of the outer rainband while the boundary layer continues to respond to the change above. The coupling of the boundary layer and middle-upper atmosphere gradually leads to the formation of the secondary eyewall. As the secondary wind and vorticity maxima strengthen, so does the associated frictional updraft. Meanwhile, a moat region facilitated by compensating subsidence from the primary eyewall begins to form to separate the two eyewalls. At Stage IV, the gradual strengthening of the secondary eyewall and the eventual weakening of the original primary eyewall complete the eyewall replacement cycle (Figure 18d).

The partial eyewall replacement cycle analysis suggests that when the outside rainband fails to adjust the outer core wind field at the right time to couple the boundary process, the secondary eyewall formation will be hindered by the failure of establishing a clear moat region that can separate the low-middle level secondary updraft maximum from the primary eyewall updraft, which will lead to the merger of the two updrafts instead of a full replacement cycle. The importance of radial distance between inner eyewall and outer rainband to SEF was also noted in previous studies of *Zhu and Zhu* [2015] and *Zhu et al.* [2015]. In addition, the frictional updraft in the potential SEF region is markedly weaker and therefore is less able to influence the convection.

We used a diagnostic boundary layer model, forced by the azimuthal-mean gradient wind field from the WRF simulation, to help interpret the evolution of the boundary layer flow in the WRF simulations. The diagnostic model accurately reproduces the WRF azimuthal-mean flow within and immediately above the inflow layer during the SEF period, except that it slightly underestimates the strength of the secondary circulation, likely due to its neglect of effect of moisture. It therefore appears that the boundary layer flow is well approximated as the response to forcing from above, via the pressure field, and that it is reasonable to regard the boundary layer as being slaved to the parent vortex as in *Kepert and Nolan* [2014].

The diagnosed boundary layer flow includes the four main features of the WRF simulation: the strengthening inflow near the surface, the supergradient flow near the developing outer eyewall, the outflow immediately aloft, and the secondary updraft. Several previous studies have discussed a chain of causality, in which the wind field expansion causes the increased inflow, which causes the enhanced supergradient flow in the upper boundary layer, which causes the outflow, which causes horizontal convergence and the updraft. However, the diagnostic steady state model is able to reproduce all of these features from knowledge only of the gradient wind field. Each of these features must therefore be caused by some characteristic of the gradient wind, specifically, a region of locally increased vorticity. We have shown that this characteristic is an outer local vorticity maximum. The idealized simulations of *Kepert* [2013], as well our comparison of WRF and the diagnostic model herein, show that these four features are best regarded as the collective response of the boundary layer flow to the vorticity perturbation, rather than as individual elements in a causal chain. That perspective carries the considerable advantage that it predicts where, within the broad overall wind expansion, the boundary layer contribution to SEF occurs. Nevertheless, the SEF clearly involves processes throughout much of the depth of the troposphere. It commences in the mid-upper troposphere and subsequently extends downward, whereupon the boundary layer becomes involved.

References

Abarca, S. F., and K. L. Corbosiero (2011), Secondary eyewall formation in WRF simulations of Hurricanes Rita and Katrina (2005), *Geophys. Res. Lett.*, *38*, L07802, doi:10.1029/2011GL047015.

Abarca, S. F., and M. T. Montgomery (2013), Essential dynamics of secondary eyewall formation, *J. Atmos. Sci.*, *70*, 3216–3230.

Black, M. L., J. F. Gamache, F. D. Marks, C. E. Samsury, and H. E. Willoughby (2002), Eastern Pacific Hurricanes Jimena of 1991 and Olivia of 1994: The effect of vertical shear on structure and intensity, *Mon. Weather Rev.*, *130*, 2291–2312.

Chen, S. S., J. A. Knaff, and F. D. Marks Jr. (2006), Effects of vertical wind shear and storm motion on tropical cyclone rainfall asymmetries deduced from TRMM, *Mon. Weather Rev.*, *134*, 3190–3208.

Dunion, J. P. (2011), Rewriting the climatology of the tropical North Atlantic and Caribbean Sea atmosphere, *J. Clim.*, *24*, 893–908.

Eliassen, A., and M. Lystad (1977), The Ekman layer of a circular vortex: A numerical and theoretical study, *Geophys. Norv.*, *31*, 1–16.

Fang, J., and F. Zhang (2012), Effect of beta shear on simulated tropical cyclones, *Mon. Weather Rev.*, *140*, 3327–3346.

Gao, K., and I. Ginis (2014), On the generation of roll vortices due to the inflection point instability of the hurricane boundary layer flow, *J. Atmos. Sci.*, *71*, 4292–4307.

Hawkins, J. D., M. Helveston, T. F. Lee, F. J. Turk, K. Richardson, C. Sampson, J. Kent, and R. Wade (2006), Tropical cyclone multiple eyewall characteristics, paper 6B.1 presented at 27th Conference on Hurricane and Tropical Meteorology, Am. Meteorol. Soc., Monterey, Calif. [Available at http://ams.confex. com/ams/27Hurricanes/techprogram/paper_108864.htm.]

Houze, R. A., Jr., S. S. Chen, B. F. Small, W.-C. Lee, and M. M. Bell (2007), Hurricane intensity and eyewall replacement, *Science*, *315*, 1235–1239.

Huang, Y.-H., M. T. Montgomery, and C.-C. Wu (2012), Concentric eyewall formation in Typhoon Sinlaku (2008). Part II: Axisymmetric dynamical processes, *J. Atmos. Sci.*, *69*, 662–674.

Judt, F., and S. S. Chen (2010), Convectively generated vorticity in rainbands and formation of the secondary eyewall in Hurricane Rita of 2005, *J. Atmos. Sci.*, *67*, 3581–3599.

Judt, F., S. S. Chen, and J. Berner (2016), Predictability of tropical cyclone intensity: Scale-dependent forecast error growth in high-resolution stochastic kinetic-energy backscatter ensembles, *Q. J. R. Meteorol. Soc.*, *142*, 43–57.

Kepert, J. D. (2001), The dynamics of boundary layer jets within the tropical cyclone core, Part I: Linear theory, *J. Atmos. Sci.*, *58*, 2469–2484.

Kepert, J. D. (2010a), Comparing slab and height-resolving models of the tropical cyclone boundary layer. Part I: Comparing the simulations, *Q. J. R. Meteorol. Soc.*, *136*, 1689–1699, doi:10.1002/qj.667.

Kepert, J. D. (2010b), Comparing slab and height-resolving models of the tropical cyclone boundary layer. Part II: Why the simulations differ, *Q. J. R. Meteorol. Soc.*, *136*, 1700–1711, doi:10.1002/qj.685.

Kepert, J. D. (2012), Choosing a boundary layer parameterization for tropical cyclone modeling, *Mon. Weather Rev.*, *140*, 1427–1445.

Kepert, J. D. (2013), How does the boundary layer contribute to eyewall replacement cycles in axisymmetric tropical cyclones?, *J. Atmos. Sci.*, *70*, 2808–2830.

Kepert, J. D., and D. S. Nolan (2014), Reply to "Comments on 'How does the boundary layer contribute to eyewall replacement cycles in axisymmetric tropical cyclones?'", *J. Atmos. Sci.*, *71*, 4692–4704.

Kepert, J. D., and Y. Wang (2001), The dynamics of boundary layer jets within the tropical cyclone core. Part II: Nonlinear enhancement, *J. Atmos. Sci.*, *58*, 2485–2501.

Kossin, J. P., and M. DeMaria (2016), Reducing operational hurricane intensity forecast errors during eyewall replacement cycles, *Weather Forecast.*, *31*, 601–608.

Kossin, J. P., and M. Sitkowski (2009), An objective model for identifying secondary eyewall formation in hurricanes, *Mon. Weather Rev.*, *137*, 876–892.

Kuo, H.-C., C.-P. Chang, Y.-T. Yang, and H.-J. Jiang (2009), Western North Pacific typhoons with concentric eyewalls, *Mon. Weather Rev.*, *137*, 3758–3770.

Kuo, H.-C., W. H. Schubert, C.-L. Tsai, and Y.-F. Kuo (2008), Vortex interactions and barotropic aspects of concentric eyewall formation, *Mon. Weather Rev.*, *136*, 5183–5198.

Lorenz, E. N. (1963), Deterministic nonperiodic flow, *J. Atmos. Sci. 20*, 130–141.

Maclay, K. S., M. DeMaria, and T. H. Vonder Haar (2008), Tropical cyclone inner-core kinetic energy evolution, *Mon. Weather Rev.*, *136*, 4882–4898.

Menelaou, K., M. K. Yau, and Y. Martinez (2012), On the dynamics of the secondary eyewall genesis in Hurricane Wilma (2005), *Geophys. Res. Lett.*, *39*, L04801, doi:10.1029/2011GL050699.

Montgomery, M. T., and R. J. Kallenbach (1997), A theory for vortex Rossby-waves and its application to spiral bands and intensity changes in hurricanes, *Q. J. R. Meteorol. Soc.*, *123*, 435–465.

Moon, Y., and D. S. Nolan (2010), The dynamic response of the hurricane wind field to spiral rainband heating, *J. Atmos. Sci.*, *67*, 1779–1805.

Moon, Y., D. S. Nolan, and M. Iskandarani (2010), On the use of two-dimensional incompressible flow to study secondary eyewall formation in tropical cyclones, *J. Atmos. Sci.*, *67*, 3765–3773.

Nolan, D. S. (2011), Evaluating environmental favorableness for tropical cyclone development with the method of point-downscaling, *J. Adv. Model. Earth Syst.*, *3*, M08001, doi:10.1029/2011MS000063.

Nolan, D. S., and L. D. Grasso (2003), Three-dimensional, nonhydrostatic perturbations to balanced, hurricane-like vortices. Part II: Symmetric response and nonlinear simulations, *J. Atmos. Sci.*, *60*, 2717–2745.

Nolan, D. S., and M. T. Montgomery (2002), Nonhydrostatic, three-dimensional perturbations to balanced, hurricane-like vortices. Part I: Linearized formulation, stability, and evolution, *J. Atmos. Sci.*, *59*, 2989–3020.

Qiu, X., and Z.-M. Tan (2013), The roles of asymmetric inflow forcing induced by outer rainbands in tropical cyclone secondary eyewall formation, *J. Atmos. Sci.*, *70*, 953–974.

Rozoff, C. M., D. S. Nolan, J. P. Kossin, F. Zhang, and J. Fang (2012), The roles of an expanding wind field and inertial stability in tropical cyclone secondary eyewall formation, *J. Atmos. Sci.*, *69*, 2621–2643.

Sitkowski, M., J. Kossin, and C. M. Rozoff (2011), Intensity and structure changes during hurricane eyewall replacement cycles, *Mon. Weather Rev.*, *139*, 3829–3847.

Stern, D. P., J. L. Vigh, D. S. Nolan, and F. Zhang (2015), Revisiting the relationship between eyewall contraction and intensification, *J. Atmos. Sci.*, *72*, 1283–1306.

Sun, Y., Y. Jiang, B. Tan, and F. Zhang (2013), The governing dynamics of the secondary eyewall formation of Typhoon Sinlaku (2008), *J. Atmos. Sci.*, *70*, 3818–3837.

Tao, D., and F. Zhang (2015), Effects of vertical wind shear on the predictability of tropical cyclones: Practical versus intrinsic limit, *J. Adv. Model. Earth Syst.*, *7*, 1534–1553, doi:10.1002/2015MS000474.

Wang, X., Y. Ma, and N. E. Davidson (2013), Secondary eyewall formation and eyewall replacement cycles in a simulated hurricane: Effect of the net radial force in the hurricane boundary layer, *J Atmos. Sci.*, *70*, 1317–1341.

Williams, G. J., R. K. Taft, B. D. McNoldy, and W. H. Schubert (2013), Shock-like structures in the tropical cyclone boundary layer, *J. Adv. Model. Earth Syst.*, *5*, 338–353.

Williams, G. J. (2015), The effects of vortex structure and vortex translation on the tropical cyclone boundary layer wind field, *J. Adv. Model. Earth Syst.*, *7*, 188–214, doi:10.1002/2014MS000299.

Willoughby, H. E., J. A. Clos, and M. G. Shoreibah (1982), Concentric eye walls, secondary wind maxima, and the evolution of the hurricane vortex, *J. Atmos. Sci.*, *39*, 395–411.

Wu, C.-C., Y.-H. Huang, and Z. Tan (2016), Secondary eyewall formation in tropical cyclones, in *Dynamics and Predictability of Large-Scale, High-Impact Weather and Climate Events*, chap. 13, pp. 168–175, Cambridge.

Zhang, F., and D. Tao (2013), Effects of vertical wind shear on the predictability of tropical cyclones, *J. Atmos. Sci., 70*, 975–983.

Zhang, J. A., F. D. Marks, M. T. Montgomery, and S. Lorsolo (2011), An estimation of turbulent characteristics in the low-level region of intense Hurricanes Allen (1980) and Hugo (1989), *Mon. Weather Rev., 139*, 1447–1462.

Zhu, P., Z. D. Zhu, S. Gopalakrishnan, R. Black, F. D. Marks, V. Tallapragada, J. A. Zhang, X. Zhang, C. Gao (2015), Impact of subgrid-scale processes on eyewall replacement cycle of tropical cyclones in HWRF system, *Geophys. Res. Lett., 42*, 10,027–10,036, doi:10.1002/2015GL066436.

Zhu, Z., and P. Zhu (2014), The role of outer rainband convection in governing the eyewall replacement cycle in numerical simulations of tropical cyclones, *J. Geophys. Res. Atmos., 119*, 8049–8072, doi:10.1002/2014JD011899.

Zhu, Z., and P. Zhu (2015), Sensitivity of eyewall replacement cycle to model physics, vortex structure, and background winds, *J. Geophys. Res. Atmos., 120*, 590–622, doi:10.1002/2014JD021899.